Probing coherent charge fluctuations in $YBa_2Cu_3O_{6+x}$ at wavevectors outside the light cone

A. von Hoegen[1], M. Fechner[1], M. Först[1], J. Porras[2], B. Keimer[2], M. Michael[3],
E. Demler[3], A. Cavalleri[1,4]

[1] *Max Planck Institute for the Structure and Dynamics of Matter, Hamburg, Germany*

[2] *Max Planck Institute for Solid State Research, Stuttgart, Germany*

[3] *Department of Physics, Harvard University, USA*

[4]*Department of Physics, University of Oxford, UK*

The possible existence of phase-incoherent superconductivity in the normal state of cuprates is one of the grand unsolved problems of modern condensed matter physics. Optical spectroscopy shows that long-range superconducting correlations disappear at T_c, although other momentum-integrated probes provide evidence for residual coherence in the normal state. Here, we use nonlinear TeraHertz spectroscopy to excite and probe coherent charge fluctuations in $YBa_2Cu_3O_{6+x}$ at frequencies and wavevectors that lie outside the light cone accessed by linear optics. In the superconducting state, we show that three-wave mixing between one optically driven phonon and two Josephson Plasma Polaritons excites coherent c-axis supercurrents at 2.4 THz and at in-plane wavevectors $q_y > 1000$ cm^{-1}. As T_c is crossed, these finite momentum supercurrent oscillations evolve continuously into a seemingly identical charge fluctuation mode, which survives up to the pseudogap temperature T^*. We argue that these results are best explained by the existence of short-range superconducting fluctuations throughout the pseudogap phase of $YBa_2Cu_3O_{6+x}$.

The far-infrared optical properties of high-T_c cuprates display more than one signature of superconductivity, including a number of resonances that reflect Josephson tunneling between CuO_2 planes[1,2]. Figure 1 displays the frequency-dependent c-axis energy-loss function $L(\omega) = -Im(1/(\varepsilon_1 + i\varepsilon_2))$ (Figure 1a) and the frequency-dependent optical conductivity $\sigma_1(\omega)$ (Figure 1b), measured in $YBa_2Cu_3O_{6.5}$ above and below the superconducting transition temperature $T_c = 53$ K (grey curve, T = 300 K; red curve, T = 10 K)[3]. Long range superconducting coherence is evidenced in these spectra by two peaks in the loss function, observed at the so-called Longitudinal Josephson Plasma frequencies $\nu_{JPR1} = 0.9$ THz and $\nu_{JPR2} = 14.2$ THz. One additional peak is observed in the real part of the optical conductivity $\sigma_1(\omega)$ at $\nu_T = 10.2$ THz, reflecting a transverse Josephson Plasma mode separated from ν_{JPR2} by a 4-THz wide reststrahlen band[3,4,5,6]. Consistent with the in-plane optical properties in this and other compounds[7,8], the disappearance of superconductivity is evidenced here most directly by the temperature-dependent 0.9-THz loss function peak (Figure 1c), which vanishes at T_c. Note that this peak has a different temperature dependence when compared to all the phonon resonances, which exhibit anomalies at T_c but remain finite and approximately temperature independent in the normal state (see Figure 1d)[4,9].

Other features associated with the superconducting condensate, such as the 10.2-THz transverse mode observed in $\sigma_1(\omega)$, have been shown to survive up to temperatures higher than T_c[10,11], and interpreted as indicative of short-range superconducting correlations surviving within the bilayers of $YBa_2Cu_3O_{6+x}$. Furthermore, other probes that are sensitive to momentum integrated responses, which include the superconducting Nernst effect[12,13,14,15,16] and measurements of electrical noise[17], provide evidence of residual coherence in the normal state.

In this work, we used TeraHertz three wave mixing to study superconducting fluctuations in $YBa_2Cu_3O_{6+x}$ at wavevectors that lie outside the light cone. The excitation geometry is shown in Figure 2a. A femtosecond 17-THz-frequency mid-infrared pulse with stable carrier-envelope phase

offset[18,19] and with polarization aligned along the c-axis of $YBa_2Cu_3O_{6+x,}$ was used to resonantly drive lattice vibrations that modulated the position of the apical oxygen atoms[3] (see Figure 2a). These large amplitude phonon oscillations can be described as a spatially homogenous excitation at the center of the Brillouin zone ($q_x = 0,\ q_y = 0$). The phonon coordinate $Q_{IR}(t)$ follows the equation of motion of a linear damped harmonic oscillator driven by the laser field: $\ddot{Q}_{IR} + 2\gamma_{IR}\dot{Q}_{IR} + \omega_{IR}^2 Q_{IR} = Z^* E(t)$. In this equation, Z^* is the Born effective charge tensor appropriate for each phonon resonance, ω_{IR} is the angular frequency and γ_i the dissipation constant for the phonon. The pulsed laser electric field is $E(t) = E_0 \sin(\omega_{IR} t) \cdot \exp(-t^2/T^2)$.

The relevant interlayer superconducting tunneling modes are described as dispersive Josephson Plasma Polaritons, collective modes of layered superconductors that arise from coupling between the supercurrents and electro-magnetic fields. In bilayer $YBa_2Cu_3O_{6+x}$, two plasma polariton modes are found, a lower energy mode that involves current flow between bilayers, and a higher energy one involving intra-bilayer supercurrents (see Figure 2).

To derive the equations of motion for these Josephson Plasma Polaritons when these are coupled to the driven lattice vibrations, one first needs to supplement Maxwell equations with the relations between the supercurrents and electromagnetic fields. The latter can be obtained directly from the kinetic energies of the interlayer tunneling and in-plane superflow, referred to here as E_{Jtun} and E_{Jplane}, respectively. The expression for these energies is $E_{Jtun} = -J_{n,n+1}\cos\left[\theta_n - \theta_{n+1} - \frac{2e}{c}\int_{z_n}^{z_{n+1}} A_z dz\right]$ and $E_{Jplane} = \frac{1}{2}\rho_s v_s^2$. Here, $\theta_n(x,y,t)$ is the order parameter within each layer n, ρ_s denotes the local superfluid density and $v_s = \nabla\theta_{x,y} - \frac{2e}{c}A$ is the in-plane superfluid velocity, which itself is a function of the in-plane order parameter gradient $\nabla\theta_{x,y}$ and of the vector potential A. In these expressions, $2e$ is the Cooper pair charge and c the speed of light.

The apical oxygen phonons excited by the pump are infrared-active and hence symmetry odd, and modify the local superfluid densities in a bilayer structure in a way that is antisymmetric with respect to the two layers (see Figs. 2a and 2b), $\delta\rho_{s\{1,2\}} \propto \pm Q_{IR}$. The effect of these vibrations on the in-plane superflow is then to increase and decrease the kinetic energy E_{Jplane} in neighbouring planes in an oscillatory fashion, and can be written as (see Supplementary Materials for details):

$$\delta E_{Jplane} = \delta\rho_{s1} v_{s1}^2 + \delta\rho_{s2} v_{s2}^2 \propto Q_{IR}(t)(v_{s1} - v_{s2})(v_{s1} + v_{s2})$$

The two types of finite-momentum tunneling modes are excited with $J_1 \sim v_{s1} - v_{s2}$ and $J_2 \sim v_{s1} + v_{s2}$, respectively. Physically, c-axis currents J_1 and J_2 are driven by the lattice excitation because the changes in the in-plane kinetic energy also involve perturbed in-plane gradients of the order parameter phase $\nabla\theta$, which then makes the c-axis tunneling dependent on the in-plane coordinate. The equations of motion for the plasmons are then

$$\ddot{J}_1 + 2\gamma_{J_1}\dot{J}_1 + \omega_{J_1}^2(q_{x1}, q_{y1})J_1 = -aq^2 Q_{IR}(t)J_2$$
$$\ddot{J}_2 + 2\gamma_{J_2}\dot{J}_2 + \omega_{J_2}^2(q_{x2}, q_{y2})J_2 = -aq^2 Q_{IR}(t)J_1$$

where $\omega_{J_1}(q_{x1}, q_{y1})$ describe the in-plane equilibrium dispersion of the Josephson Plasma Polariton.

These equations predict three-wave mixing between the apical oxygen phonons and the upper and lower Josephson Plasma Polaritons, leading to the excitation of damped harmonic oscillations for J_1 and J_2 at finite momenta along the two-dimensional dispersion of Figure 2c, with a driving term $aq^2 Q_{IR}(t)J_{2,1}$. Note that the driving term depends on the momentum of the plasma polariton as q^2,

it is zero for long wavelengths ($q = 0$) but naturally couples to supercurrents at finite in-plane wavevectors. The two equations of motion predict that the phonon excites pairs of Josephson Plasma Polaritons with frequencies that satisfy $\omega_1 + \omega_2 = \omega_{IR}$, driven at opposite in-plane momenta ($q_{x1} = -q_{x2}$ or $q_{y1} = -q_{y2}$).

A numerical solution of these equations of motion is shown in the color-coded dispersion of Figure 2c and 2d. There, the three-wave mixing process is shown to couple preferentially the driven phonon to plasma polaritons at in-plane momenta q_y ~ 1500 cm^{-1} ($\lambda \sim 6.7$ μm) where phase matching can take place. Because of the pump optical field is screened in the propagation direction (perpendicular to the optical surface) over a skin depth of ~1.5 μm, phase matching is inefficient along *x* (see Figure 2c). This results in the excitation of pairs of high (intra bilayer) and low (inter bilayer) frequency Josephson Plasma Polaritons, which propagate along the optical surface $J_1(\omega_1, +q_y)$ and $J_2(\omega_2, -q_y)$, or $J_1(\omega_1, -q_y)$ and $J_2(\omega_2, +q_y)$. The corresponding responses in time and frequency are shown in Figures 2e and 2f, which display the calculated momentum-integrated time profile and a combined spectrum for the three fields involved J_1, J_2 and Q_{IR}, which resonate at 2.4 THz, 14 THz and 17 THz.

Note that other mechanisms can couple the driven phonon to Josephson Plasma Polaritons, such as those that descend from the modification of the interlayer Josephson coupling strength, for example by modifying the dielectric constant between the bilayers[20]. However, symmetry requires that this coupling scales with Q_{IR}^2 and is to be thought of as a four-wave mixing process between two phonons and two Josephson Plasma Polaritons, which is weaker, not frequency resonant and hence not taken into account at this stage. Furthermore, at the field strengths used in these experiments the lattice response is expected to involve also high-order phonon harmonics[21] and coupling between otherwise normal lattice modes[22,23,24,25]. However, for the purposes of the present discussion, these lattice-only nonlinearities are also neglected.

The prediction of a three-wave mixing between apical oxygen phonon and two Josephson Plasma Polaritons was validated in pump probe experiments on $YBa_2Cu_3O_{6.48}$ that combined the excitation of phonon oscillations at 17 THz frequency with time resolved reflectivity measurements from the excited surface using a near-infrared (800-nm) optical pulse of 30 fs duration (see Figure 3a). The probe pulse was polarized along the same *c*-axis direction of the mid-infrared excitation and was delayed in time with respect to the pump. The 30-fs duration of the optical probe corresponded to a Nyquist sampling frequency of approximately 17 THz, and could resolve the amplitudes of all the plasma modes and of the driven phonons without deconvolution.

As shown in Figure 3, we recorded two quantities as a function of time. First, we measured the time-dependent linear reflectivity $\Delta R(t)$ (Figure 3b), which exhibited coherent oscillations associated with zone-center totally-symmetric modes of A_g symmetry through Stimulated Ionic Raman Scattering[24]. Second, we measured the time-dependent second harmonic intensity $\Delta I_{SH}(t)$, which was generated by the 800 nm probe below the surface (Figure 3c)[26]. The measurement of $\Delta I_{SH}(t)$ enabled detection of all the coherently excited infrared-active optical phonons and the Josephson Plasma Polaritons[27,28,29], which are symmetry-odd and hence modulated the second-order susceptibility $\Delta\chi^2(t)$ in time (see Supplementary Materials). As shown schematically in Figure 3a, for a time dependent second harmonic occurring at momentum q_y=1500 cm^{-1} (see calculation in Figure 2d), one expects second-harmonic radiation diffracted over a broad set of angles centered around $\Delta\theta = 1.8$ degrees from the specular reflection. A lens was used to collect all the second harmonic scattered from the sample and to focus it on a photo-multiplier. An interference filter blocked the linear reflection at 800 nm wavelength (see Supplementary Materials).

Figure 4 reports the measured oscillations in second harmonic intensity in the low temperature superconducting state ($T = 5\ K \ll T_c = 53\ K$), extracted from the traces similar to that reported in

Figure 3c by subtracting the slowly varying non-oscillatory contributions to the signal. In Figure 4a we display measurements obtained in the superconducting state for the weakest phonon excitation (500 kV/cm peak electric field). The corresponding spectrum (Figure 4b) displays two groups of peaks. Two different phonon modes at 17 and 20 THz were observed (shaded in yellow), which were directly driven by the pump. Indeed, although the pump was tuned to be resonant with the 17 THz mode, its finite frequency bandwidth (17 THz ± 5 THz) covered a second apical oxygen mode at higher frequency. At lower frequencies, we detected two Josephson Plasma Polariton modes (shaded in red and magenta) at 2.3 and 14 THz, as predicted by the theory in Figure 2f, and indicating that even at this relatively small excitation field the nonlinear coupling between the phonon and the plasma oscillations was activated.

The results for strong excitation (7 MV/cm) are reported in Figures 4c and 4d. The same two sub-harmonic peaks at 2.3 and 14 THz are observed, with larger amplitude than those reported in Figures 4a and 4b. Note that for this excitation field a number of additional peaks (shaded in grey in Figure 4d) were observed at 4, 6, 8 and 10 THz, which correspond to known infrared-active phonons at or near zero momentum. These are excited by a higher order, phononic *four*-wave mixing process[25], not discussed here (see Supplementary Materials for details).

In Figure 5a, we report the pump-field dependence of the 2.3-THz Josephson Plasma Polariton amplitude. As both phonon and plasmon amplitudes were measured simultaneously with the phase sensitive probe, $J_1(Q_{IR})$ was extracted directly from the data. The appropriateness of our model is underscored by the plot in Figure 5b, which displays the same scaling in the calculated J_1 at several Q_{IR} values.

We next turn to the temperature dependence of J_1. As the low frequency Josephson Plasma mode participating in the three-wave mixing process disappears at T_c in the linear optical spectra of Figure 1, one would expect the oscillations in second harmonic to disappear at the same

temperature. This expectation is contradicted by our experiments. Figures 6a and 6b show the temporal oscillations and corresponding spectra for three representative base temperatures of 5 K (red), 300 K (light red) and 440 K (grey). The same modes reported in Figure 4 are observed here, and are found to extend far above the equilibrium critical temperature T_c, and to vanish only above T = 400 K. A more extensive temperature dependence is displayed for the 2.3-THz coherent mode in the range between 5 K and 440 K (Figure 6c), and compared to the response of the equilibrium Josephson Plasma mode at 0.9 THz, which disappears at T_c. As in the equilibrium spectra, this temperature dependence is different from that of the infrared-active phonons (Figure 6d), which exhibit only an anomaly at T_c and a temperature independent amplitude in the normal state. Finally, we report $J_1(Q_{IR})$ measured at two temperatures, T = 5 K and T = 300 K, in which we find a similar exponential growth as that reported in Figure 5a. This scaling is characteristic of parametric three-wave mixing and is further validation of the predictions discussed above.

The same experiments discussed above for $YBa_2Cu_3O_{6.48}$ were repeated for $YBa_2Cu_3O_{6.65}$. Identical features were observed as those discussed above, including the excitation of Josephson Plasma Polaritons at 2.8 THz and 15 THz. These frequencies were higher than those observed for $YBa_2Cu_3O_{6.48,}$ because in $YBa_2Cu_3O_{6.65}$ the plasma polaritons were shifted to the blue due to the larger c-axis superfluid density (see Supplementary Material) and exhibited a slightly different dispersion due to the stronger in-plane inductive coupling. As observed in $YBa_2Cu_3O_{6.48}$, the plasma modes for $YBa_2Cu_3O_{6.65}$ also extended far above T_c.

Figure 6f displays the temperature dependences of the low-frequency Josephson Plasmon Polariton amplitude for the two doping levels, along with an empirical mean-field fit $\propto \sqrt{1 - T/T'}$ that yields two critical temperatures $T' \approx 380$ K and $T' \approx 280$ K for $YBa_2Cu_3O_{6.48}$ and $YBa_2Cu_3O_{6.65,}$ respectively. Strikingly, for these two doping values the measured T' values agree well with the corresponding pseudogap temperatures T^*[16,30,31,32], pictorially displayed in Figure 6g.

The body of evidence reported above provides useful perspective for the physics of high-T_c cuprates. Finite momentum (q_y > 1000 cm^{-1}) interlayer tunneling fluctuations, occurring at frequencies of 2.4 and 2.8 THz for $YBa_2Cu_3O_{6.48}$ and $YBa_2Cu_3O_{6.65,}$ respectively, were observed below T_c. However, unlike the zero momentum peaks detected in linear measurements (see Figure 1), these TeraHertz modes were not observed to disappear at T_c but extended smoothly into the pseudogap phase and up to room temperature.

Whilst the measurement of these excitations alone is *per se* not a conclusive demonstration of superconductivity in the normal state, the fact that these fluctuations are connected smoothly across T_c points to a similarity between the superconducting mode below T_c and the charge oscillations above it. Furthermore, the observation of normal state interlayer tunneling with relaxation rates far in excess of 1 ps is difficult to reconcile with incoherent charge dynamics characteristic of the pseudogap phase of cuprates.

Note also that no other symmetry-odd mode could explain these oscillations. The lowest frequency optical phonon in this material is approximately at 4.5 THz, and remains at approximately the same frequency for the range of q_y wavevectors reported here. Equally, acoustic phonons dispersing out from q = 0 are far too weakly dispersive to hybridize with the charge modes of Figure 2c and 2d at these wavevectors, as the speed of sound is many orders of magnitude smaller than the group velocity of the Josephson Plasma Polaritons discussed here (approximately 1% of the speed of light). Finally, as shown in the temperature dependence of Figure 6c, the 2.4 THz oscillations disappear at T*, whereas all optical phonon peaks remain constant with temperature.

We propose that the coherent charge modes observed in the normal state are more convincingly explained by hypothesizing the existence of high temperature superconducting fluctuations at frequencies of a few TeraHertz and correlation lengths of several microns[33], possibly connected to condensation at finite momentum[34,35,36,37]. These fluctuations lie at frequencies and wavevectors

outside the light cone, and hence have remained undetected to date. We also note that the higher frequency intra-bilayer fluctuations near 12 THz lie at the edge of the light cone, which may explain why these are observed in linear optical spectroscopy at temperatures above T_c,[10] whilst the lower energy inter-bilayer modes are not.

Note that the experimental method reported here is not generally applicable to all compounds and to all dopings, as it relies on the frequency matching between the apical oxygen excitation and the two plasma polaritons. For example, in the case of doping levels closer to optimal doping we did not find evidence for any charge modes, as the three-wave frequency resonance is not fulfilled (see data for $YBa_2Cu_3O_{6.92}$ in the Supplementary Materials). Hence, the insight gathered here should be validated by more comprehensive methods such as Resonant Inelastic X-ray Scattering[38,39] and high-resolution Electron Energy Loss probes[40]. However, our experiments open up new perspectives of frequency resonant wave mixing as a new means to study cooperative phenomena in quantum materials. Finally, we note that the results reported here may provide a microscopic explanation for the observations reported in previous work, in which similar types of phonon excitation were shown to give rise to characteristic reflectivity edges and conductivities associated with superconducting behavior [41,42,43].

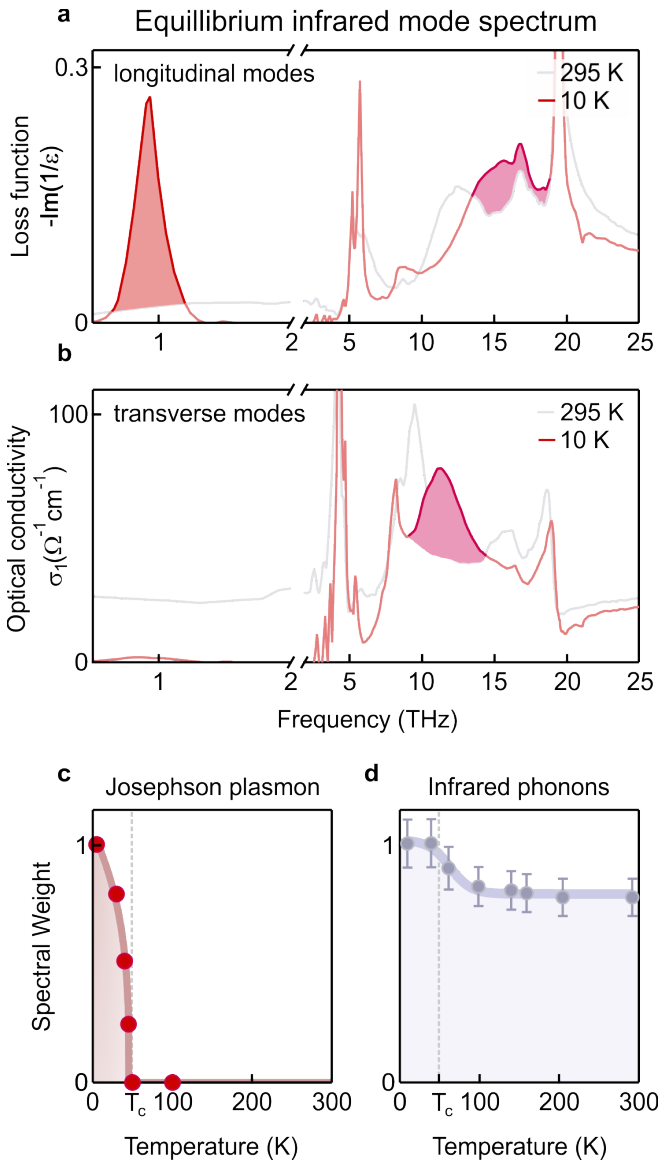

Figure 1| Linear THz optical properties of $YBa_2Cu_3O_{6.5}$. a and **b**, Energy loss function $L(\omega) = -Im(1/(\varepsilon_1 + i\varepsilon_2))$ and real part of the optical conductivity $\sigma_1(\omega)$ along the *c*-axis of $YBa_2Cu_3O_{6.5}$ for temperatures of 10 K (red lines) and 295 K (grey lines), respectively. The red and magenta shaded peaks highlight the Josephson Plasma modes described in the text. The remaining resonances can be ascribed to infrared-active lattice vibrations (see Refs. 3 and 42). **c** and **d**, Temperature dependence of the oscillator strengths of the low-frequency Josephson plasmon (red-shaded peak at 0.9 THz in panel a) and of the infrared-active phonon modes.

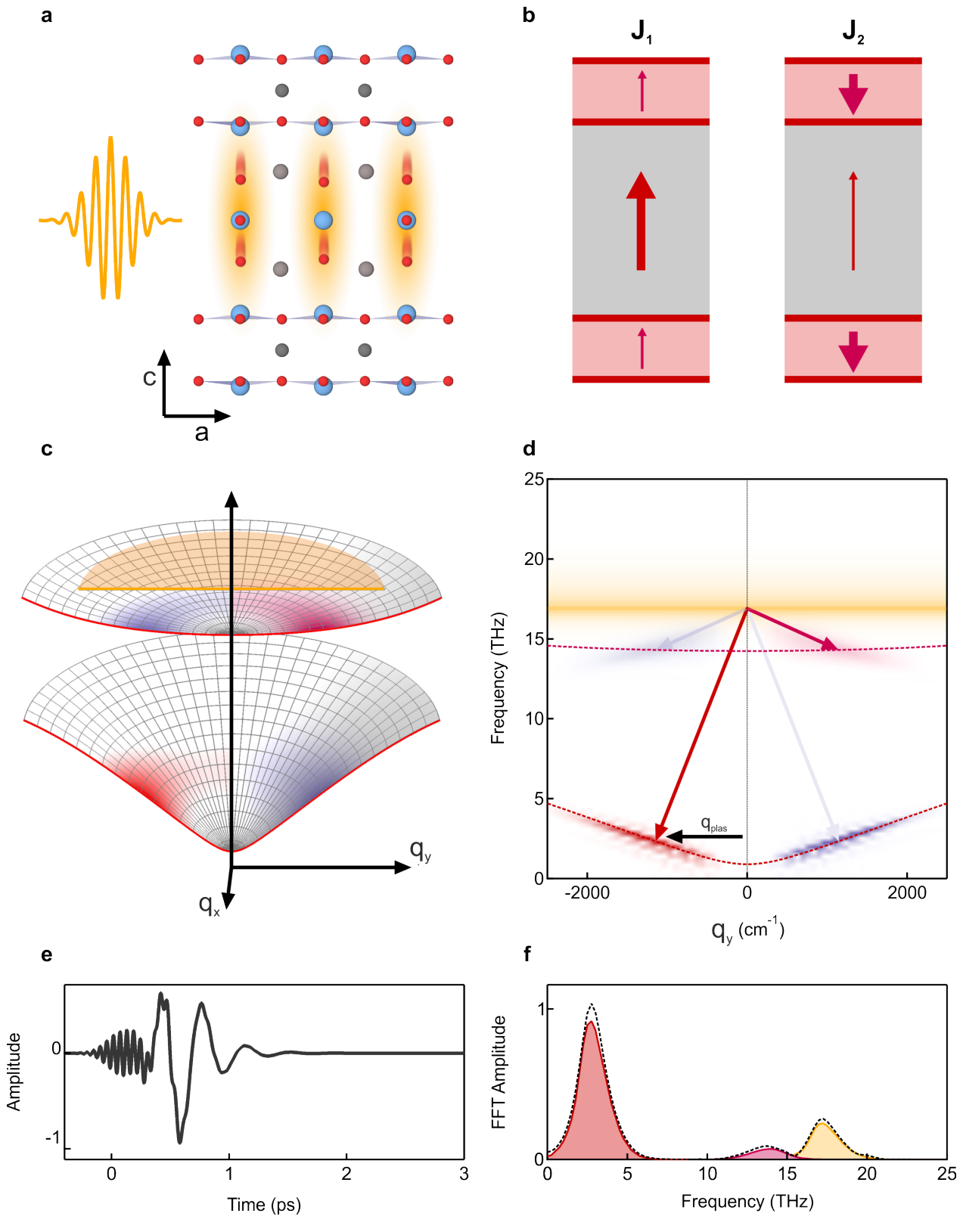
a
c
a
b
J1
J2
c
qy
qx
d
Frequency (THz)
qplas
qy (cm-1)
e
Amplitude
Time (ps)
f
FFT Amplitude
Frequency (THz)

Figure 2| THEORY. Nonlinear excitation of Josephson plasmons at finite momentum. a, An intense mid-infrared pulse, propagating along the crystal *a*-axis and polarized along *c,* resonantly excites oscillations of the apical oxygen atoms (yellow-shaded motion). **b**, Sketch of the two Josephson Plasma modes at q = 0, with the supercurrents oscillating in-phase (J_1) or out-of-phase (J_2) for the low and high frequency mode, respectively. The thicknesses of the arrows indicate the supercurrent strengths between and within the bilayers. **c**, Dispersion of the two Josephson Plasma Polaritons along the in-plane momenta q_x and q_y, with the red lines being a cut through the $q_x = 0$ plane. The apical oxygen phonon mode at 17 THz (yellow) does not disperse along either direction. The red and blue surfaces represent nonlinearly excited Josephson Plasma Polaritons in response to the resonant drive of the apical oxygen phonon at q = 0. The response vanishes along q_x, parallel to the light propagation direction. **d**, Detailed insight into the simulation results along q_y (for q_x = 0). The driven phonon with zero momentum excites a pair of Josephson Plasmon Polaritons, J_1 and J_2, with opposite wavevectors q_y and frequencies that add up to the phonon frequency. The two processes for mirrored momentum transfer are shown as red and blue arrows, respectively. **e** and **f**, Time-dependent momentum-integrated Josephson Plasma oscillations, obtained by solving the equations of motion described in the text. The corresponding Fourier amplitude spectrum shows peaks at $\nu_1 = 2.3$ THz (red) and $\nu_2 = 14$ THz (magenta), which are plotted together with the Fourier spectrum of the driven phonon at 17 THz (yellow).

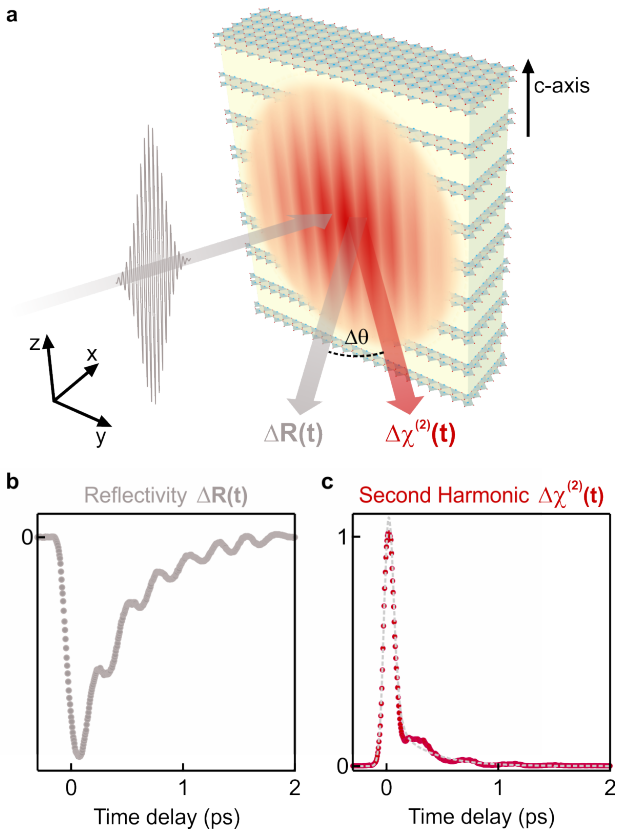

Figure 3| EXPERIMENT. Optical probe geometry and time-resolved changes. a, Schematic of the probe geometry. The 800-nm pulse was polarized along the $YBa_2Cu_3O_{6.48}$ crystal *c*-axis and perpendicular to the CuO_2-planes. Light at the fundamental reflects from the sample at the specular direction (grey arrow) whilst second harmonic frequencies (red arrow) exit at a small angle $\Delta\theta$ from there, due to diffraction from the spatially modulated nonlinear polarization that arises from the finite-momentum Josephson Plasma Polaritons (red stripes, $1/q_{plas} \sim 6.7$ μm). **b**, Time resolved linear reflectivity at 800 nm wavelength, showing coherent modulations due to fully symmetric Raman phonon modes. **c**, Time resolved second harmonic intensity at 400 nm wavelength (red circles) and a numerical fit to the non-oscillatory component of the signal (dashed line).

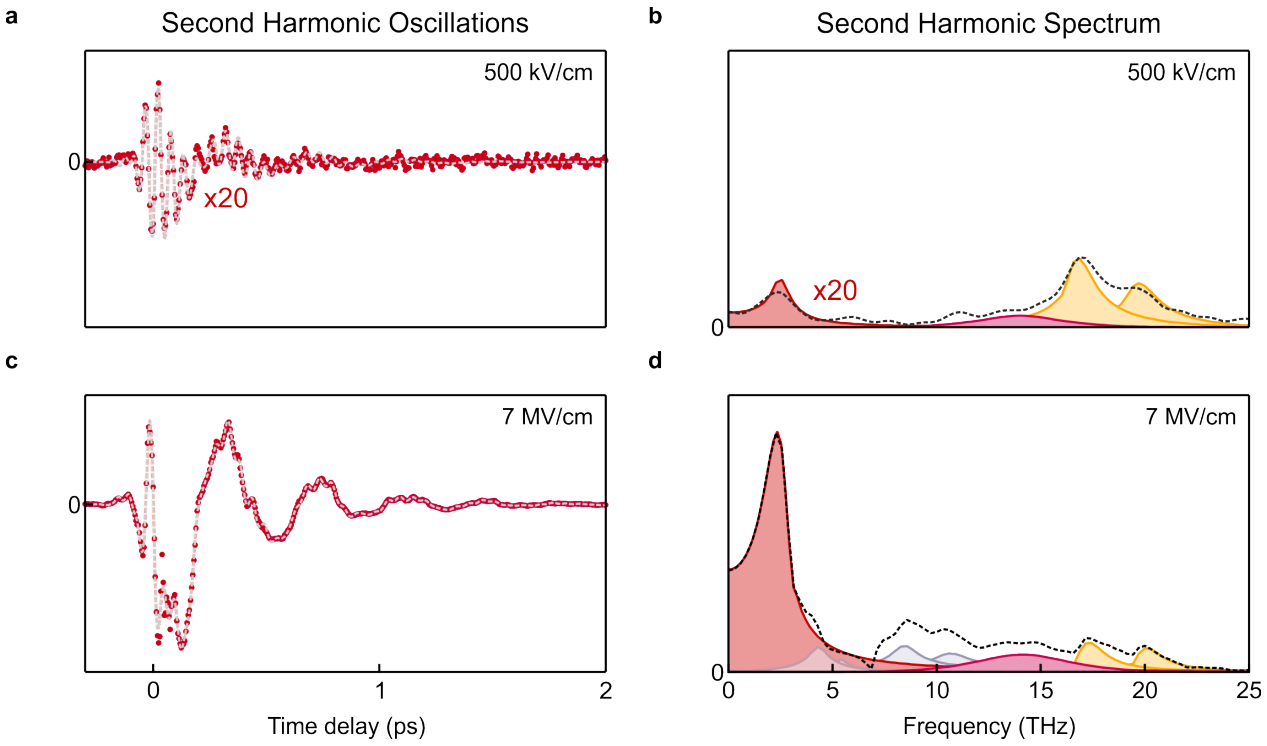

Figure 4| EXPERIMENT. Coherent oscillations in second harmonic intensity in the superconducting state. a and **b,** Coherent signal of the SH intensity at low excitations fields (E = 500 kV/cm) and the corresponding Fourier amplitude spectrum at T = 5 K, well below the critical temperature T_C = 48 K. The peaks at ν_1 = 2.3 THz and ν_2 = 14 THz (red and magenta) are ascribed to coherent oscillations of the Josephson Plasma modes. The high frequency oscillations at 17 and 19.5 THz (yellow peaks) are coherent symmetry breaking apical oxygen vibrations, resonantly driven by the excitation pulse. **c**, Coherent SH response at higher excitations fields (E = 7 MV/cm) at the same temperature. **d**, Fourier amplitude spectrum corresponding to the strong field excitation, showing the same coherences of panel a and b. The grey peaks label additional phonons nonlinearly coupled to the resonantly driven lattice modes.

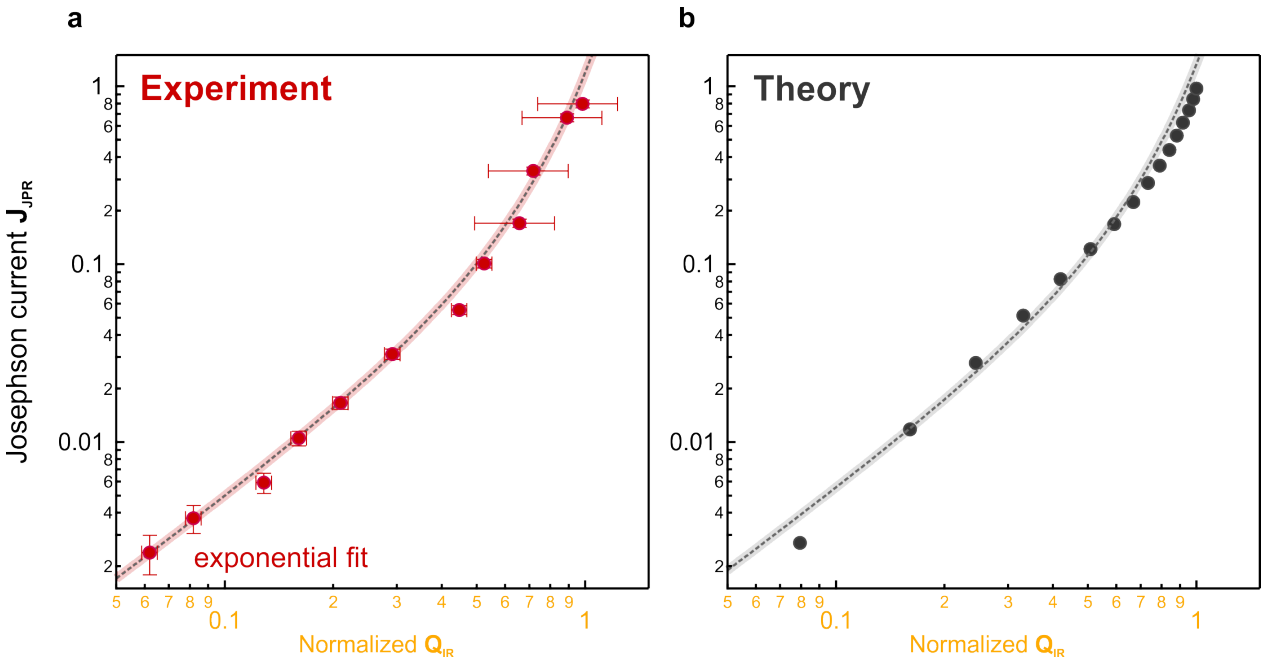

Figure 5| EXPERIMENT. Excitation field dependence of the low-frequency Josephson Plasma Polariton. a, Measured amplitude of the low frequency Josephson Plasmon J_{JPR} plotted as a function of the driven apical oxygen vibration amplitude Q_{IR}, both extracted from similar data as shown in Figure 4, for different strengths of the mid-infrared excitation field. The dashed line is an exponential fit $J(Q) = a \cdot (e^{\frac{Q^b}{\tau}} - 1)$ to the data. Error bars represent the standard deviation σ of the amplitudes extracted by numerical fits. **b**, Theoretically expected amplitudes J_{JPR} plotted against Q_{IR}, both obtained from the calculations presented in Figure 2 for different mid-infrared excitation field strengths. The dashed line is the same fit as of panel a, scaled by a constant factor.

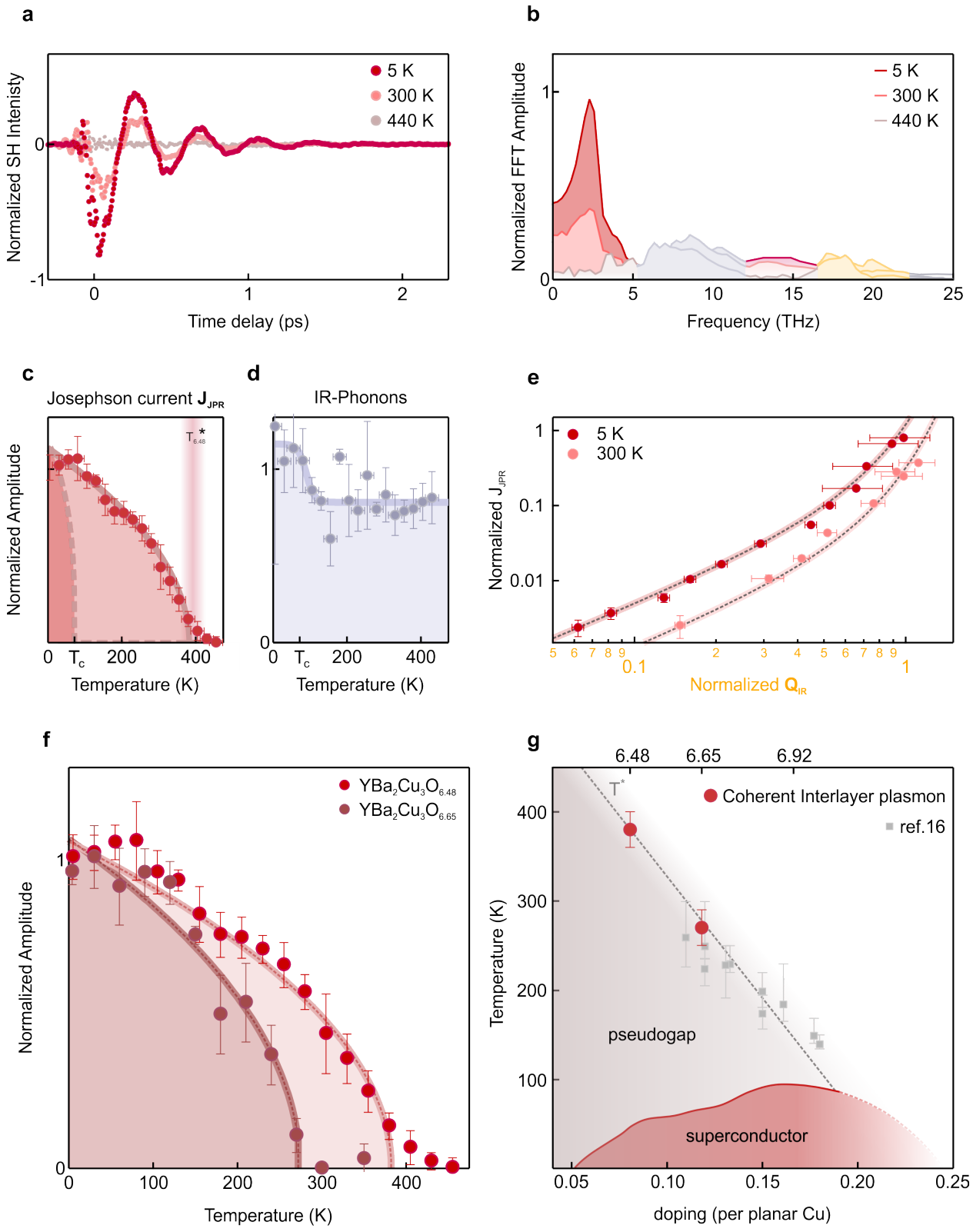
a
Normalized SH Intenisty
5 K
300 K
440 K
Time delay (ps)
b
Normalized FFT Amplitude
5 K
300 K
440 K
Frequency (THz)
c
Josephson current J_JPR
Normalized Amplitude
T_c
Temperature (K)
d
IR-Phonons
Temperature (K)
e
5 K
300 K
Normalized J_JPR
Normalized Q_IR
f
YBa2Cu3O6.48
YBa2Cu3O6.65
Normalized Amplitude
Temperature (K)
g
6.48
6.65
6.92
T*
Coherent Interlayer plasmon
ref.16
pseudogap
superconductor
Temperature (K)
doping (per planar Cu)

Figure 6| EXPERIMENT. Temperature dependence of the coherent Josephson Plasmons. a, Coherent plasma oscillations in the SH Intensity of $YBa_2Cu_3O_{6.48}$ for three different temperatures (5 K, red; 300 K, light red; 440 K, grey). **b**, Fourier amplitude spectra to the curves shown in panel a, divided into the Josephson Plasma modes (red and magenta), the driven apical oxygen modes (yellow) and the nonlinear lattice response (grey). **c**, Temperature dependence of the nonlinearly driven low frequency plasma amplitude (red dots) fitted by a mean-field law $\propto \sqrt{1 - T/T^*}$ (red line), together with the temperature dependence of the equilibrium Josephson Plasma mode in the superconducting state (dashed line). **d**, Temperature dependence of the amplitude of the nonlinearly coupled infrared-active phonons. The grey line is a guide to the eye. **e**, Excitation strength dependence at low temperature (red circles, 5 K) and high temperature (light red circles, 300 K), similar to the plots shown in Figure 5a. **f**, Temperature dependent Josephson Plasma amplitudes of $YBa_2Cu_3O_{6.48}$ (red circles) and $YBa_2Cu_3O_{6.65}$ (dark red circles). The lines are fits to the data with a mean-field approach $\propto \sqrt{1 - T/T'}$, yielding $T' = 380$ K for $YBa_2Cu_3O_{6.48}$ and $T' = 280$ K for $YBa_2Cu_3O_{6.65}$. **g**, Phase-diagram of $YBa_2Cu_3O_{6+x}$, showing the regions of equilibrium superconductivity (red) and the pseudogap (grey). The temperatures T', above which the coherent Josephson Plasmon oscillations of our study disappear, are shown as red circles. They agree well with the pseudogap temperature T^* extrapolated from Nernst effect measurements (grey line)[16]. Error bars were obtained by repeating our experiments under equal conditions and represent a standard deviation σ.

References

[1] D. Basov, S. I. Woods, A. Katz, E. J. Singley, R. C. Dynes, M. Xu, D. G. Hinks, C. C. Homes and M. Strongin, Sum rules and interlayer conductivity of high-T_c cuprates. *Science* **283**, 49-52 (1999).

[2] K. Tamasaku, Y. Nakamura and S. Uchida, Charge dynamics across the CuO_2 plasnes in $La_{(2-x)}Sr_xCuO_4$. *Physical Review Letters* **69**, 1455-1458 (1992).

[3] C. C. Homes, T. Timusk, D. A. Bonn, R. Liang and W. N. Hardy, Optical properties along the c-axis of $YBa_2Cu_3O_{6+x}$, for x = 0.50 → 0.95 evolution of the pseudogap. *Physica C* 254, 265-280 (1995).

[4] D. Munzar, C. Bernhard, A. Golnik, J. Humlicek and M. Cardona, Anomalies of the infrared-active phonons in underdoped $YBa_2Cu_3O_y$ as evidence for the intra-bilayer Josephson effect. *Solid State Communications* 112, 365-369 (1999).

[5] M. Grüninger, D. van der Marel, A. A. Tsvetkov and A. Erb, Observation of out-of-phase bilayer plasmon in $YBa_2Cu_3O_{7-\delta}$. *Physical Review Letters* 84, 1575-1578 (2000).

[6] D. van der Marel and A. Tsvetkov, Transverse optical plasmons in layered superconductors. *Czechoslovak Journal of Physics* 46, 3165-3168 (1996).

[7] J. Corson, R. Mallozzi, J. Orenstein, J. N. Eckstein and I. Bozovic, Vanishing of phase coherence in underdoped $Bi_2Sr_2CaCu_2O_{8+\delta}$," *Nature* 398, 221-223 (1999).

[8] L. S. Bilbro, R. Valdes Aguilar, G. Logvenov, O. Pelleg, I. Bozovic and N. P. Armitage, Temporal correlations of superconductivity above the transition temperature in $La_{2-x}Sr_xCuO_4$ probed by terahertz spectroscopy. *Nature Physics* 7, 298-302 (2011).

[9] J. Schützmann, S. Tajima, S. Miyamoto, Y. Sato and R. Hauff, Doping and temperature dependence of c-axis optical phonons in $YBa_2Cu_3O_y$ single crystals. *Physical Review B* 52, 13665 (1995).

[10] A. Dubroka, M. Rössle, K. W. Kim, V. K. Malik, D. Munzar, D. N. Basov, A. A. Schafgans, S. J. Moon, C. T. Lin, D. Haug, V. Hinkov, B. Keimer, T. Wolf, J. G. Storey, J. L. Tallon and C. Bernhard, Evidence of a pecursor superconducting phase at temperatures as high as 180 K in $RBa_2Cu_3O_{7-\delta}$ (R = Y, Gd, Eu) superconducting crystals from infrared spectroscopy. *Physical Review Letters* 106, 047006 (2011).

[11] B. Sopik, J. Chaloupka, A. Dubroka, C. Bernhard and D. Munzar, Evidence for precursor superconducting pairing above T_c in underdoped cuprates from an analysis of the in-plane infrared response. *New Journal of Physics* 17, 053022 (2015).

[12] Z. A. Xu, P. Ong, Y. Wang, T. Kakeshita and S. Uchida, Vortex-like excitations and the onset of superconducting phase fluctuation in underdoped $La_{2-x}Sr_xCuO_4$. *Nature* 406, 486-488 (2000).

[13] Y. Wang, Z. A. Xu, T. Kakeshita, S. Uchida, S. Ono, Y. Ando and N. P. Ong, Onset of the vortex like Nernst signal above T_c in $La_{2-x}Sr_xCuO_4$ and $Bi_2Sr_{2-y}La_yCuO_6$. *Physical Review B* 64, 224519 (2001).

[14] J. Chang, N. Doiron-Leyraud, F. Laliberté, R. Daou, D. LeBoeuf, B. J. Ramshaw, R. Liang, D. A. Bonn, W. N. Hardy, C. Proust, I. Sheikin, K. Behnia and L. Taillefer, Nernst effect in the cuprate superconductor $YBa_2Cu_3O_y$: Broken rotational and translational symmetries. *Physical Review B* 84, 014507 (2011).

[15] O. Cyr-Choinière, R. Daou, F. Laliberte, C. Collignon, S. Badoux, D. LeBoeuf, J. Chang, B. J. Ramshaw, D. A. Bonn, W. N. Hardy, R. Liang, J.-Q. Yan, J.-G. Cheng, J.-S. Zhou, J. Goodenough, S. Pyon, T. Takayama, H. Takagi, N. Doiron-Leyraud and L. Taillefer, Pseudogap temperature T^* of cuprate superconductors from the Nernst effect. *Physical Review B* 97, 064502 (2018).

[16] R. Daou, J. Chang, D. LeBoeuf, O. Cyr-Choinière, F. Laliberté, N. Doiron-Leyraud, B. J. Ramshaw, R. Liang, D. A. Bonn, W. N. Hardy and L. Taillefer, Broken rotational symmetry in the pseudogap phase of a high-T_c superconductor. *Nature* 463, 519-522 (2010).

[17] P. Zhou, L. Chen, Y. Liu, I. Sochnikov, A. T. Bollinger, M.-G. Han, Y. Zhu, X. He, I. Božović and D. Natelson, Electron pairing in the pseudogap state revealed by shot noise in copper oxide junctions. *Nature* 572, 493-496 (2019).

[18] A. Sell, A. Leitenstorfer and R. Huber, Phase-locked generation and field-resolved detection of widely tunable terahertz pulses with amplitudes exceeding 100 MV/cm. *Optics Letters* 33, 2767-2769 (2008).

[19] C. Manzoni, M. Först, H. Ehrke and A. Cavalleri, Single-shot detection and direct control of carrier phase drift of midinfrared pulses. *Optics Letters* 35, 757-759 (2010).

[20] S. Denny, Y. Laplace, S. Clark, A. Cavalleri, D. Jaksch, Proposed parametric cooling of bilayer superconductors with THz radiation *Physical Review Letters* **114**, 137001 (2015)

[21] A. von Hoegen, R. Mankowsky, M. Fechner, M. Först and A. Cavalleri, Probing the interatomic potential of solids with strong-field nonlinear phononics. *Nature* 555, 79-82 (2018).

[22] M. Först, C. Manzoni, S. Kaiser, Y. Tomioka, Y. Tokura, R. Merlin and A. Cavalleri, Nonlinear phononics as an ultrafast route to lattice control. *Nature Physics* 7, 854-856 (2011).

[23] R. Mankowsky, A. Subedi, M. Först, S. Mariager, M. Chollet, H. Lemke, J. S. Robinson, J. M. Glownia, M. P. Minitti, A. Frano, M. Fechner, N. A. Spaldin, T. Loew, B. Keimer, A. Georges and A. Cavalleri, Nonlinear lattice dynamics as a basis for enhanced superconductivity in $YBa_2Cu_3O_{6.5}$. *Nature* 516, 71-73 (2014).

[24] R. Mankowsky, M. Först, T. Loew, J. Porras, B. Keimer and A. Cavalleri, Coherent modulation of the $YBa_2Cu_3O_{6+x}$ atomic structure by displacive stimulated ionic Raman scattering. *Physical Review B* 91, 094308 (2015).

[25] A. Subedi, A. Cavalleri and A. Georges, Theory of nonlinear phononics for coherent light control of solids. *Physical Review B* 89, 220301(R) (2014).

[26] M. Fiebig, V. V. Pavlov and R. V. Pisarev, Second-harmonic generation as a tool for studying electronic and magnetic structures of crystals: review. *Journal of the Optical Society of America B* 22, 96-118 (2005).

[27]M. Cardona, R. K. Chang, G. Güntherodt, M. B. Long and H. Vogt, Light Scattering in Solids II. Topics in Applied Physics (Springer, Berlin, Heidelberg, 1982).

[28] V. N. Denisov, B. N. Mavrin and V. B. Podobedov, Hyper-Raman scattering by vibrational excitations in crystals, glasses and liquids. *Physics Reports* 151, 1-92 (1987).

[29] Z. Cheng, Quantum field theory of hyper-Raman scattering in piezoelectric crystals. *Physical Review B* 66, 165101 (2002).

[30] Y. Lubashevsky, L. Pan, T. Kirzhner, G. Koren and N. P. Armitage, Optical birefringence and dichroism of cuprate superconductors in the THz regime. *Physical Review Letters* 112, 147001 (2014).

[31] B. Fauqué, Y. Sidis, V. Hinkov, S. Pailhès, C. T. Lin, X. Chaud and P. Bourges, Magnetic order in the pseudogap phase of High-T_c superconductors. *Physical Review Letters* 96, 197001 (2006).

[32] A. Shekhter, B. J. Ramshaw, R. Liang, W. N. Hardy, D. A. Bonn, F. F. Balakirev, R. D. McDonald, J. B. Betts, S. C. Riggs and A. Migliori, Bounding the pseudogap with a line of phase transitions in $YBa_2Cu_3O_{6+\delta}$. *Nature* 498, 75-77 (2013).

[33] V.J. Emery, S.A. Kivelson Importance of phase fluctuations in superconductors with small superfluid density *Nature* 374, 434 (1995).

[34] E. Berg *et al.*, Dynamical Layer Decoupling in a Stripe-Ordered High-T_c Superconductor. *Phys. Rev. Lett.* **99**, 127003 (2007).

[35] P. A. Lee, "Amperean Pairing and the Pseudogap Phase of Cuprate Superconductors," *Physical Review X,* 4, 031017 (2014).

[36] S. Rajasekaran, J. Okamoto, L. Mathey, M. Fechner, V. Thampy, G.D. Gu, A. Cavalleri, Probing optically silent superfluid stripes in cuprates *Science* 369, 575-579 (2018).

[37] S.D. Edkins, A. Kostin, K. Fujita, A.P. MacKenzie, H. Eisaki, S. Uchida, S. Sachdev, M.J. Lawler, Magnetic field induced pair density wave state in the cuprate vortex halo *Science* 396, 976-980 (2019).

[38] W. S. Lee, I. M. Vishik, K. Tanaka, D. H. Lu, T. Sasagawa, N. Nagaosa, T. P. Devereaux, Z. Hussain and Z.-X. Shen, Abrupt onset of a second energy gap at the superconducting transition of underdoped Bi2212. *Nature* 450, 81-84 (2007).

[39] M. Hepting, L. Chaix, E. W. Huang, R. Fumagalli, Y. Y. Peng, B. Moritz, K. Kummer, N. B. Brookes, W. C. Lee, M. Hashimoto, T. Sarkar, J.-F. He, C. R. Rotundu, Y. S. Lee, R. L. Greene, L. Braicovich, G. Ghiringhelli, Z.-X. Shen, T. P. Devereaux and W. S. Lee, Three-dimensional collective charge excitations in electron-doped copper oxide superconductors. *Nature* 563, 374-378 (2018).

[40] M. Mitrano, A. A. Husain, S. Vig, A. Kogar, M. S. Rak, S. I. Rubeck, J. Schmalian, B. Uchoa, J. Schneeloch, R. Zhong, G. D. Gu and P. Abbamonte, Anomalous density fluctuations in a strange metal. *Proceedings of the National Academy of Sciences* 115, 5392-5396 (2018).

[41] S. Kaiser, C. R. Hunt, D. Nicoletti, W. Hu, I. Gierz, H. Y. Liu, M. Le Tacon, T. Loew, D. Haug, B. Keimer, and A. Cavalleri, Optically induced coherent transport far above T_c in underdoped $YBa_2Cu_3O_{6+\delta}$. *Physical Review B* 89, 184516 (2014).

[42] W. Hu, S. Kaiser, D. Nicoletti, C. R. Hunt, I. Gierz, M. C. Hoffmann, M. L. Tacon, T. Loew, B. Keimer and A. Cavalleri, Optically enhanced coherent transport in $YBa_2Cu_3O_{6.5}$ by ultrafast redistribution of interlayer coupling. *Nature Materials* 13, 705-711 (2014).

[43] B. Liu, M. Först, M. Fechner, D. Nicoletti, J. Porras, B. Keimer and A. Cavalleri, Two pump frequency resonances for light-induced superconductivity in $YBa_2Cu_3O_{6.5}$. arXiv 1905.08356 (2019).

Supplementary Materials for

Probing coherent charge fluctuations in $YBa_2Cu_3O_{6+x}$ at wavevectors outside the light cone

A. von Hoegen[1], M. Fechner[1], M. Först[1], J. Porras[2], B. Keimer[2], M. Michael[3], E. Demler[3], A. Cavalleri[1,4]

[1]*Max Planck Institute for the Structure and Dynamics of Matter, Hamburg, Germany*
[2]*Max Planck Institute for Solid State Research, Stuttgart, Germany*
[3]*Department of Physics, Harvard University, USA*
[4]*Department of Physics, University of Oxford, UK*

Sample preparation

The samples are detwinned single crystals of $YBa_2Cu_3O_{6+\delta}$ grown in Y-stabilized zirconium crucibles. The hole doping of the Cu-O planes was adjusted by controlling the oxygen content of the CuO chain layer through annealing in flowing O_2 and subsequent rapid quenching.[44] The critical temperatures of the superconducting transitions were determined by dc magnetization measurements (T_c = 45 K for $YBa_2Cu_3O_{6.48}$, T_c = 67 K for $YBa_2Cu_3O_{6.65}$ and T_c = 94 K for $YBa_2Cu_3O_{6.92}$).

For the optical experiments, *bc*-surfaces of the single crystals were polished to optical grade with a final lapping step at 100 nm grid size. The samples were then mounted into an optical cryostat where their temperature could be controlled between 10 and 450 K.

Optical setup

The carrier envelope phase (CEP) stable mid-infrared pump pulses were obtained by mixing the two signal beams from two optical parametric amplifiers, which were seeded by the same white light and pumped by 30-fs pulses at 800 nm wavelength and 1 kHz repetition rate. The pulses were 150 fs long and centered at 17.5 THz with a bandwidth of 5 THz. The driven dynamics in the $YBa_2Cu_3O_{6+x}$ samples were probed by time-delayed replicas of the 800-nm

pulses, in non-collinear geometry with an angle of ~17° to the normal-incidence mid-infrared pump (see Fig. S1).

The pump induced polarization rotation of the 800-nm pulses, reflected from the $YBa_2Cu_3O_{6+x}$ samples, was measured by detecting the time-resolved difference signal of two intensity-balanced photodiodes placed behind a half-wave plate and a Wollaston prism.

The light fields generated at the second harmonic frequency (SH) at 400 nm wavelength were separated from the fundamental beam behind the sample by a dichroic mirror and then detected by a photo multiplier tube.

Both schemes probe the material up to a depth of approximately ~0.1 μm, much smaller than the penetration depth of the mid-infrared excitation of about 1.5 μm.[3]

SHG probing of the plasma polariton and phonon dynamics by hyper-Raman scattering

The electric polarization in a material generated by a probe light field E_ω can be expanded as

$$P = \alpha E + \frac{1}{2}\beta E^2 + \cdots = P^{(1)} + P^{(2)} + \cdots,$$

where α and β are the polarizability and hyper-polarizability, respectively.

The first term $P^{(1)}$ describes the linear optical response. For example, the change of polarizability α by a non-polar mode is responsible for Raman scattering.[45,46] The term $P^{(2)}$ is responsible for second-order nonlinear optical processes, like second harmonic generation. A polar mode that carries an electric-dipole moment inside the crystal modifies the hyper-polarizability β proportional to its amplitude J [47,48,49]

$$\Delta\beta = \frac{\partial\beta}{\partial J}J,$$

known as hyper-Raman scattering.

The interaction of the polar mode with the probe light can be described by the wave equation

$$\frac{\partial^2 E}{\partial z^2} - \frac{n^2}{c^2}\frac{\partial^2 E}{\partial t^2} = \frac{\partial \beta}{\partial J}\frac{\partial^2 J E_{probe}^2}{\partial t^2},$$

where n is the refractive index of the material and c the vacuum speed of light. E_{probe} denotes the probe laser field at angular frequency ω_{probe}, i.e. of the fundamental 800-nm pulses, $J(t+\tau) = J_0 \cdot \sin(\Omega \cdot (t+\tau))$ is the time-dependent amplitude of the polar mode, and τ the time delay between the pump and probe pulses. The right-hand side of the above equation is equivalent to a time dependent second order nonlinear polarization $P^{(2)} = \frac{\partial \beta}{\partial Q} J(t) E_{probe}^2$, which generates light close to the second harmonic frequency of the incoming probe. The frequency spectrum of the scattered light then becomes

$$E(\omega) = E_{probe}(\omega) + \frac{c \cdot n}{4}\omega\frac{\partial \beta}{\partial J} \cdot l \cdot J_0 \cdot (E_{probe}(2\omega + \Omega) \cdot \exp(\mathrm{i}\Omega \cdot \tau) - E_{probe}(2\omega - \Omega) \cdot \exp(-\mathrm{i}\Omega \cdot \tau))$$

where l is the interaction length between the probe beam and the polar excitation J. It contains the unperturbed probe spectrum $E_{\mathrm{probe}}(\omega)$ and sidebands generated at frequencies $2\omega_{\mathrm{probe}} \pm \Omega$. The phase sensitive detection of these sidebands, for example achieved by spectral interference with a local oscillator on the detector, carries information about both, the phase and amplitude of the polar excitation.

In the SH measurement, the detected light is generated in a thin layer l of about 100 nm below the sample surface. The propagation of the Josephson plasmon along the surface creates a fringe pattern with a spatial period $1/q_{plas}$. The minima and maxima of this pattern emit SH light with phase shifts of 180° as becomes apparent from the linear dependence on J in the nonlinear polarization $P^{(2)}$ above. Spatial integration of this pattern by a large probe beam then results in zero specular reflection intensity.

However, the SH intensity measured in the present experiments also contains the first diffraction order which fulfils the condition

$$\sin(\theta_1) + \sin(\theta_i) = \frac{\lambda}{2} q_{plas}$$

where θ_i denotes the incidence angle with respect to the surface normal, $\lambda = 400$ nm the SH wavelength and θ_1 the exit angle of the diffracted radiation. The resulting diffraction angle differs from the specular reflection by $\Delta\theta = 1.8°$, which is small enough to allow collimation with a lens placed closely behind the sample and detection of the SH light by the photo-multiplier.

Analysis of the time-resolved SHG signals

The measured time-resolved SH intensity signals (see for example Fig. 3c of the manuscript) were fitted by the product of (i) a Gaussian envelope to map the nonlinear optical mixing of pump and probe electric fields at time delay zero (electric field induced second harmonic generation, EFISH) and (ii) a step function of finite width, multiplied by a decaying exponential, i.e. $A(\tau) = A \cdot (1 + \mathrm{erf}\,((\tau - \tau_0)/\sigma)) \cdot \exp\,(-\gamma(\tau - \tau_0))$, to describe the exponentially decaying background signal. Subtraction of this slowly varying background revealed the coherent oscillations shown in Figures 4a and c of the main text for low- and high fluence excitation. The oscillatory signals can be divided into sets of three exponentially decaying oscillators: the driven polar phonons, the nonlinearly coupled phonons, and the nonlinearly coupled Josephson plasmons (see Fig. S2). Here, the phonon frequencies were constrained to values measured by linear infrared spectroscopy.[3]

Doping dependence of the Josephson Plasma oscillations

The time-resolved SHG experiments on $YBa_2Cu_3O_{6.48}$ presented in the main text were complemented by a set of measurements on two differently doped compounds, namely underdoped $YBa_2Cu_3O_{6.65}$ (T_C = 67 K) and optimally doped $YBa_2Cu_3O_{6.92}$ (T_C = 94 K). Figure S3 shows the coherent signal oscillations extracted from the raw data for all three doping levels, measured at 5 K temperature and 7 MV/cm peak electric field, together with their corresponding Fourier amplitude spectra. The set of nonlinearly coupled phonons (grey peaks)

remains unchanged for all three doping levels, whereas the Josephson Plasma frequencies shift with increasing doping to higher frequencies, tracking the blue shift of the Josephson Plasma edges in the equilibrium superconducting states.[41] With respect to $YBa_2Cu_3O_{6.48}$, the amplitude of the coherent plasma oscillations decreased at higher-doped $YBa_2Cu_3O_{6.65}$ and disappeared at optimally doped $YBa_2Cu_3O_{6.92}$. This can be explained by the resonance condition $\omega_{IR} = \omega_{J1}(q_{plas}) + \omega_{J2}(-q_{plas})$ for the nonlinear coupling between the resonantly driven phonon and the Josephson plasmons at finite q, which can still be fulfilled in $YBa_2Cu_3O_{6.65}$ ($\omega_{J1}(0) = 2$ THz, $\omega_{J2}(0) = 15$ THz)[3] but not in $YBa_2Cu_3O_{6.92}$ ($\omega_{J1}(0) = 7.5$ THz, $\omega_{J2}(0) = 30$ THz).[50]

Theoretical analysis of the Josephson Plasma Polariton

Analysis of the collective modes

Plasmon dispersion in a layered superconductor can be obtained by combining linearized dynamical equations for superflow currents and charges with Maxwell equations for electromagnetic fields.[51,52,53,54,55,56] The fundamental degrees of freedom are density fluctuations of the condensate $\delta\rho_{\lambda,i}(\vec{x})$, the phase of the superconducting order parameter $\phi_{\lambda,i}(\vec{x})$, and the 4-component vector potential ($V_{\lambda,i}(\vec{x}), A_{\lambda,i,z}(\vec{x})\ \vec{A}_{\lambda,i,\vec{x}}(\vec{x})$). Here i corresponds to the index of the unit cell along the c-axis, $\lambda = 1,2$ labels the number of the layer inside the unit cell, and $\vec{x}$ is the in-plane coordinate, which we will omit in the equations below for brevity. While the in-plane components of the vector potential $\vec{A}_{\lambda,i,\vec{x}}(\vec{x})$ are defined within the corresponding layers, $A_{\lambda,i,z}(\vec{x})$ is defined to be on the links between layers starting on layer $\{\lambda, i\}$ as shown in Fig. S4.

In linearized hydrodynamics, superflow currents are given by

$$j_{\lambda,i,\vec{x}} = \Lambda_s\left(\partial_{\vec{x}}\phi_{\lambda,i} - e^* A_{\lambda,i,\vec{x}}\right), \quad (1)$$

$$j_{\lambda,i,z} = j_{c\lambda}\left(\Delta_z \phi_{\lambda,i} - e^* A_{\lambda,i,z}\right). \quad (2)$$

Here $\vec{x}$ denotes the in-plane x, y components and z denotes the c-axis coordinate of the crystal. Coupling to the vector potential is given by the Cooper pair charge, $e^* = 2e$, and we work in units where $\hbar = 1$ for the rest of this section. The in-plane components of the superfluid current are defined within individual layers and have continuous gradients. The z component of the current is defined as the Josephson current between adjacent layers and has a lattice gradient which corresponds to the phase difference between adjacent layers,

$$\Delta_z \phi_{\lambda,i} = \begin{cases} (\phi_{2,i} - \phi_{1,i})/d_1, \text{for } \lambda = 1, \\ (\phi_{1,i+1} - \phi_{2,i})/d_2, \text{for } \lambda = 2 \end{cases} \quad (3)$$

The coefficient Λ_s is related to the in-plane London penetration length as $\Lambda_s = \frac{\epsilon c^2}{\lambda_L^2 (e^*)^2}$, where $\epsilon = \epsilon_r \epsilon_0$. Physically, it corresponds to the intra-layer superfluid stiffness and is proportional to the condensate density, $\Lambda_{s\lambda} \propto \rho_\lambda$. In linear analysis of the collective modes we can set $\Lambda_{s\lambda}$ to be equal to their equilibrium values since they multiply superfluid velocities, $\vec{v}_{\lambda,i} = \partial_{\vec{x}} \phi_{\lambda,i} - e^* A_{\lambda,i,\vec{x}}$, which are already first order in fluctuations. This is why we omitted the layer index for Λ_s in equation (1). Coefficients $\{j_{c,\lambda}\}$ correspond to interlayer Josephson tunneling couplings and obey $j_{c,\lambda} \propto \sqrt{\rho_1 \rho_2}$. In linearized hydrodynamics we take $j_{c,\lambda}$ to be equal to their equilibrium value and neglect corrections due to $\delta\rho_\lambda$. Both ρ_λ and $j_{c,\lambda}$ can be modified by exciting apical oxygen phonons, which results in phonon-plasmon coupling that will be discussed below. We introduce an effective Hamiltonian that describes plasmon degrees of freedom and show that its equations of motion give the correct equations for light and matter fields.

$$H = H_{pot.} + H_{kin.} + H_{EM.} \quad (4)$$

The first term in eqn. (4) describes finite compressibility of Cooper pairs and their coupling to electrostatic potential

$$H_{pot.} = \int d^2x \sum_{i,\lambda} \left\{ \frac{\gamma}{2} \delta\rho_{\lambda,i}^2 + e^* \delta\rho_{\lambda,i} V_{\lambda,i} \right\}. \tag{5}$$

Compressibility γ can be related to the Thomas-Fermi length, λ_{TF}, as $\gamma = \frac{\lambda_{TF}^2 (e^*)^2}{\epsilon}$.

The superflow kinetic energy is given by

$$H_{kin.} = \int d^2x \sum_{i,\lambda} \left\{ \frac{1}{2\Lambda_s} j_{\lambda,i,\vec{x}}^2 + \frac{1}{2j_{c,\lambda}} j_{\lambda,i,z}^2 \right\}. \tag{6}$$

For electromagnetic fields we adopt the Lorenz gauge condition

$$\frac{1}{c^2} \partial_t V_{\lambda,i} + \partial_{\vec{x}} A_{\lambda,i,\vec{x}} + \Delta_z A_{\lambda,i,z} = 0 \tag{7}$$

then the Hamiltonian for electromagnetic fields is given by

$$\begin{aligned} H_{EM} = \int d^2x \Bigg\{ & \sum_{i,\lambda} \frac{c^2}{2\epsilon} P_{V,\lambda,i}^2 + \frac{\epsilon}{2} \left(\left(\partial_{\vec{x}} V_{\lambda,i} \right)^2 + \left(\Delta_z V_{\lambda,i} \right)^2 \right) \\ & + \frac{1}{2\epsilon} P_{A_{\vec{x}},\lambda,i}^2 + \frac{\epsilon c^2}{2} \left(\left(\partial_{\vec{x}} A_{\lambda,i,\vec{x}} \right)^2 + \left(\Delta_z A_{\lambda,i,\vec{x}} \right)^2 \right) \\ & + \frac{1}{2\epsilon} P_{A_z,\lambda,i}^2 + \frac{\epsilon c^2}{2} \left(\left(\partial_{\vec{x}} A_{\lambda,i,z} \right)^2 + \left(\Delta_z A_{\lambda,i,z} \right)^2 \right) \Bigg\} \end{aligned} \tag{8}$$

Variables $\{P_{V,\lambda,i}, P_{A_{\vec{x}},\lambda,i}, P_{A_z,\lambda,i}\}$ correspond to the conjugate momenta of the scalar and vector potentials, and magnetic permeability $\mu = \mu_r \mu_0$ is included in the speed of light $c^2 = 1/\mu\epsilon$. In eqn. (8) gradients in the z direction are taken in the lattice form so, for example,

$$\Delta_z A_{\lambda,i,z} = \begin{cases} \frac{A_{1,i,z}}{d_1} - \frac{A_{2,i-1,z}}{d_2}, \text{for } \lambda = 1, \\ \frac{A_{2,i,z}}{d_2} - \frac{A_{1,i,z}}{d_1}, \text{for } \lambda = 2 \end{cases} \tag{9}$$

We use Heisenberg equations of motion (EOM) for the operators, $\partial_t \hat{O} = i[H, \hat{O}]$, to study dynamics of the fields. In deriving equations of motion we use canonical commutation relations between ρ and ϕ, V and P_V, $\vec{A}$ and $P_{\vec{A}}$, i.e. $\left[\rho_i(\vec{x}), \phi_j(\vec{x}\,')\right] = i\delta^2(\vec{x} - \vec{x}\,')\delta_{i,j}$, etc. EOM for the density and phase operators give the continuity equation and Josephson relation

$$\partial_t \delta\rho_{\lambda,i} + \partial_{\vec{x}} j_{\lambda,i,\vec{x}} + \Delta_z j_{\lambda,i,z} = 0. \tag{10}$$

$$\partial_t \phi_{\lambda,i} = -\gamma\delta\rho_{\lambda,i} - e^* V_{\lambda,i}, \tag{11}$$

By combining EOM for the electromagnetic fields ϕ, $\vec{A}$ and their conjugate momenta we obtain Maxwell's equations:

$$\left(\frac{1}{c^2}\partial_t^2 - \partial_{\vec{x}}^2 - \Delta_z^2\right) V_{\lambda,i} = \frac{e^*}{\epsilon}\delta\rho_{\lambda,i}, \tag{12a}$$

$$\left(\frac{1}{c^2}\partial_t^2 - \partial_{\vec{x}}^2 - \Delta_z^2\right) A_{\lambda,i,\vec{x}} = \frac{1}{c^2}\frac{e^*}{\epsilon} j_{\lambda,i,\vec{x}}, \tag{12b}$$

$$\left(\frac{1}{c^2}\partial_t^2 - \partial_{\vec{x}}^2 - \Delta_z^2\right) A_{\lambda,i,z} = \frac{1}{c^2}\frac{e^*}{\epsilon} j_{\lambda,i,z} \tag{12c}$$

To find collective modes we look for the solutions of equations (10), (11), (12) in the form of plane waves, $\delta\rho_{\lambda,l}(x,t) = \delta\rho_\lambda(q_{\vec{x}}, q_z, \omega)e^{i(q_x x + q_y y + q_z Dl - \omega t)}$, with similar expressions for other variables. It is convenient not to combine EOM for electromagnetic fields and their conjugate variables, so that we have first order linear differential equations of the form $\partial_t \vec{v} = \underline{\boldsymbol{M}}\,\vec{v}$. Matrix $\underline{\boldsymbol{M}}$ contains gradient operators which leads to implicit dependence on momentum $\vec{q}$. We define the characteristic polynomial for $\underline{\boldsymbol{M}}$ as $\chi(\omega) = \det\left|i\omega + \underline{\boldsymbol{M}}\right|$. Due to the Lorenz gauge used in our analysis the characteristic polynomial contains unphysical degrees of freedom. However, gauge constraint (7) guarantees that they do not couple to matter fields and the characteristic polynomial factorizes into physical and unphysical contributions, $\chi(\omega) = \chi_{phys}(\omega)\chi_{unphys}(\omega)$. Collective modes of the system can be found by solving the secular

equation $\chi_{phys}(\omega) = 0$. The two lowest energy modes correspond to the Josephson plasmons and their dispersion is shown in Fig. S5.

To express physical quantities in terms of the amplitudes of the plasmon modes we can use eigenvectors $v^{l}_{\{1,2\},q}$ of the secular equation, where components l correspond to $\delta\rho_\lambda$, ϕ_λ, V, $\vec{A}$, etc. Shown in a matrix form:

$$\begin{pmatrix} \rho_\lambda(q) \\ \vdots \\ \phi_\lambda(q) \\ \vdots \end{pmatrix} = \begin{pmatrix} v^{\delta\rho_\lambda}_{1,q} & \cdots & (v^{\delta\rho_\lambda}_{1,q})^* & \cdots \\ \vdots & & \vdots & \\ v^{\phi_\lambda}_{1,q} & & (v^{\phi_\lambda}_{1,q})^* & \\ \vdots & & \vdots & \end{pmatrix} \cdot \begin{pmatrix} b_1 \\ \vdots \\ b_1^* \\ \vdots \end{pmatrix} \qquad (13)$$

where b_1 and b_2 are amplitudes of the two plasmon modes oscillating at frequencies corresponding to their dispersion relations. The eigenvectors, $v^{l}_{\{1,2\},q}$, are defined through the EOM up to a normalization constant. Normalization is fixed through the commutation relations of canonically conjugate pairs, such as $[\rho_\lambda(q), \phi_{\lambda'}(q')] = i\delta_{q,q'}\delta_{\lambda,\lambda'}$ and commutation relations of the plasmon fields, which should correspond to bosonic creation/annihilation operators $[b_i, b^\dagger] = \delta_{i,j}$.

Phonon-plasmon interaction

The apical oxygen phonon is expected to modify the in-plane superfluid stiffness either by changing the in-plane density of carriers or by modifying their hopping. Symmetry of this mode requires that these changes are antisymmetric with respect to the two layers inside one unit cell, so that $\delta\Lambda^{phon}_{s,\{1,2\}}(t) = \pm\xi Q_{IR}(t)\Lambda_s$, where coefficient ξ characterizes the coupling strength. Changes of the interlayer Josephson currents arise from changes in the superfluid density $\delta\rho^{phon}_{\{1,2\}} = \pm\tilde{\xi}\, Q_{IR}(t)\rho$, which results in $\delta j_{c,\lambda}(t) = -\left(\tilde{\xi}\, Q_{IR}\right)^2 \frac{j_{c,\lambda}}{2\rho}$. The last equation shows that interlayer Josephson currents couple quadratically to the apical oxygen phonon and lead to four-

wave phonon/plasmon mixing. Resonant three wave mixing considered in the main text comes from phonons modifying $\Lambda_{s,\{1,2\}}$ and coupling to the in-plane current.

To derive plasmon dynamics in the presence of excited phonon mode we need to modify equation (6) to include $\delta\Lambda_{s\lambda}^{phon}$ arising due to phonons. We find

$$\delta H_{kin.} = -\xi \sum_i \int d^2x \left\{ \frac{Q_{IR}(t)}{2\Lambda_s} \left(j_{1,i,\vec{x}}^2 - j_{2,i,\vec{x}}^2\right) \right\} \tag{14}$$

The phonon mode causes a zero momentum three wave parametric process that excites pairs of plasmons at opposite momenta. Resonant processes that satisfy energy matching condition $\omega_{ph} = \omega_1(q) + \omega_2(-q)$ lead to exponential instability discussed in the main text. After projecting the modified EOM to the two the lowest eigenmodes we find equations for parametrically coupled oscillators

$$\partial_t^2 J_1(q) + 2\gamma_1 \partial_t J_1(q) + \omega_1^2(\vec{q}) J_1(q) = -q_x^2 f(\vec{q}) Q_{IR}(t) J_2(q), \tag{15a}$$

$$\partial_t^2 J_2(q) + 2\gamma_2 \partial_t J_2(q) + \omega_2^2(\vec{q}) J_2(q) = -q_x^2 f(\vec{q}) Q_{IR}(t) J_1(q) \tag{15b}$$

In writing equations (15) we added phenomenological damping constants γ_i to describe dissipation due to quasiparticles. Factors of q_x^2 in equations (15) originate from the fact that phonons couple to plasmons through the in-plane superflow kinetic energy. There is also an implicit weaker q dependence in $f(\vec{q})$ arising from projecting the interaction to the plasmon subspace, which can be derived using the $v_{\{1,2\},q}^{j_{\lambda,\vec{x}}}$ components of the eigenvectors of the secular equation. We also note that inversion symmetry forbids three-mode coupling between the phonon and Josephson plasmons in the same band.

The equation of motion for the polar phonon reads

$$\ddot{Q}_{\mathrm{IR}} + 2\gamma_{\mathrm{IR}} \dot{Q}_{\mathrm{IR}} + \omega_{\mathrm{IR}}^2 Q_{\mathrm{IR}} = Z^* E(t) - q_y^2 J_1 J_2 \,,$$

where Z^* is the coupling to the optical drive field and γ_{IR} accounts for the finite lifetime of the vibrational mode.

We solved the set of coupled equations for the phonon and plasmon dynamics by utilizing a stochastic approach, where we introduced Langevin noise on both, the Josephson plasma and phonon coordinates, to create an incoherent initial state. The final trajectories shown in the manuscript (see Figure 2e) were then computed by solving the equations of motion one million times with an algorithm based on the Euler-Maruyama method. In addition to the harmonic terms that describe the resonant driving of the polar phonon mode, we also considered higher-order (quartic) phonon anharmonicities.

Nonlinear phonon-phonon coupling

The phonon spectrum of the ortho-II structure of $YBa_2Cu_3O_{6.5}$ consists of 73 non-translational modes at the Brillouin zone center. The most relevant phonon modes for *c*-axis polarized THz and mid-infrared excitation are 13 infrared-active B_{1u} modes and 11 Raman-active A_g modes. The full lattice potential $V_{lattice}$ consists of three distinct contributions.[25,57,58]

1. The harmonic potential of each phonon mode

$$V_{harm} = \sum \frac{\omega_i^2}{2} Q_i^2,$$

with ω_i and Q_i representing the eigenfrequency and coordinate of the i-th mode, respectively.

2. The anharmonic potential containing higher-order terms of the phonon coordinates and combinations of different phonon modes

$$V_{anharm} = \sum g_{ijk} Q_i Q_j Q_k + \sum f_{iklm} Q_i Q_k Q_l Q_m,$$

with g_{ijk} and f_{iklm} indicating third and fourth order anharmonic coefficients, respectively.

3. The coupling of the resonantly driven phonon B_{1u} mode to an external electric field

$$V_{efield} = \sum Z^*_{B1u} Q_{B1u} E_{field} ,$$

with Z^*_{B1u} representing the mode effective charge.[25]

The structural dynamics are then determined by the equations of motion for each phonon mode, given by

$$\ddot{Q}_i + 2\gamma_i \dot{Q}_i + \nabla_{Q_i}(V_{harm} + V_{anharm} + V_{efield}) = 0.$$

Here γ_i is a phenomenological damping term, which accounts for contributions to the finite lifetime which are not already considered within the anharmonic potential. The equations are restricted to phonon modes at the Brillouin zone center, due to the negligible momentum of long wavelengths THz light.

First, we consider the impact of the third order terms in V_{anharm} on the lattice dynamics. Of the modes that we consider here, only the 11 A_g modes fulfill the symmetry requirements to exhibit such a third-order coupling to the driven B_{1u} mode.[23] To simplify the discussion, we consider coupling between the driven mode and a single A_g mode. The equations of motions then reduce to

$$\ddot{Q}_{\mathrm{B1u}} + \gamma \dot{Q}_{\mathrm{B1u}} + \omega^2_{B1u} Q_{B1u} + 2g Q_{B1u} Q_{Ag} = Z^*_{B1u} Q_{B1u} E_{field}$$

$$\ddot{Q}_{Ag} + \gamma_{Ag} \dot{Q}_{Ag} + \omega^2_{Ag} Q_{Ag} + g Q^2_{B1u} = 0.$$

They describe a process known as ionic Raman scattering which entails a transient displacement and superimposed oscillations of the Q_{Ag}.[22,23,24,25]

As detailed above, coherent non-polar A_g-symmetry modes can be observed by Raman scattering of a femtosecond probe pulse in the time delay dependent reflectivity changes. The amplitude spectrum of the coherently oscillating Raman modes, shown in Fig. 3b of the manuscript, is shown in Fig. S6. The frequencies of the observed modes at 3.7, 4.2 and 4.5 THz

agree with continuous-wave Raman scattering experiments and theoretical predictions of the same compound (also shown in Fig. S6).[24]

Next, we consider the implications of the quartic order terms in V_{anharm}. In addition to the A_g modes, also the B_{1u} modes fulfill the symmetry requirements for bi-quadratic coupling $Q_{IR,i}^2 Q_{IR,j}^2$ and linear cubic coupling $Q_{IR,i}^3 Q_{IR,j}$. Due to the selective resonant excitation of only one polar phonon mode, coupling between three or more modes is neglected. The corresponding anharmonic term then becomes $V_{anharm} = f_1 Q_{IR,1}^2 Q_{IR,2}^2 + f_2 Q_{IR,1}^3 Q_{IR,2} + f_3 Q_{IR,1} Q_{IR,2}^3$. The bi-quadratic term leads to a parametric amplification of the coupled phonons, as becomes apparent from the equations of motion

$$\ddot{Q}_{\mathrm{IR},1} + \gamma \dot{Q}_{\mathrm{IR},1} + (\omega_{IR,1}^2 + 2f_1 Q_{IR,2}^2) Q_{IR,1} + 3f_2 Q_{IR,1}^2 Q_{IR,2} + f_3 Q_{IR,2}^3 = Z_{IR,1}^* Q_{IR,1} E_{field}$$

$$\ddot{Q}_{\mathrm{IR},2} + \gamma \dot{Q}_{\mathrm{IR},2} + (\omega_{IR,2}^2 + 2f_1 Q_{IR,1}^2) Q_{IR,2} + f_2 Q_{IR,1}^3 + 3f_3 Q_{IR,1} Q_{IR,2}^2 = 0.$$

This parametric amplification is characterized by an exponential scaling of the coupled mode $Q_{IR,2}$ as a function of the driven mode $Q_{IR,1}$ and a parametric resonance at $\omega_{IR,1} = 2 \cdot \omega_{IR,2}$. Fig. S6 reports comprehensive calculations involving coupling between all B_{1u} modes. We scaled the corresponding amplitudes by $Z_{B1u,i}^*$ to calculate the polarization induced by each individual mode and further convolved the results with the 30-fs time resolution of the experiment. We find agreement with the experimental observations (see Fig. S7).

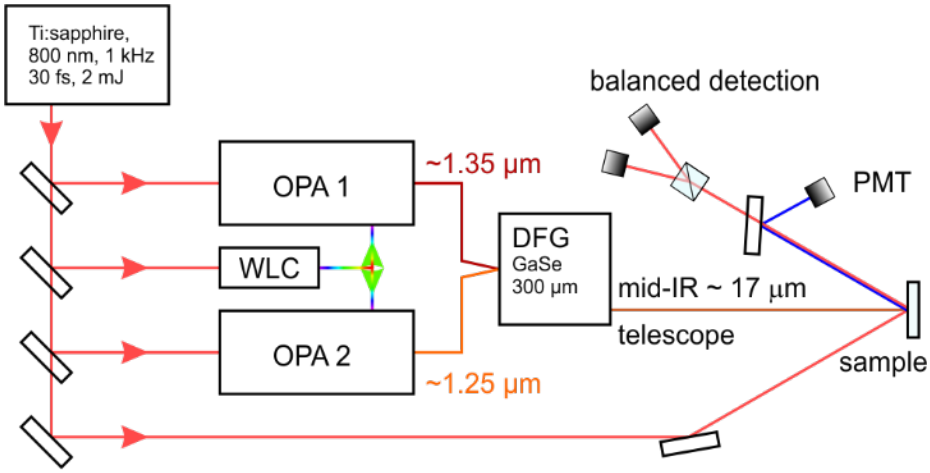

Fig. S1: Schematic drawing of the experimental setup. 30-fs pulses from a Ti:sapphire amplifier pump two optical parametric amplifiers (OPA), which are seeded by the same white light continuum (WLC) . Carrier envelope phase stable 3-µJ 150-fs pulses at 17 µm wavelength are generated by difference frequency mixing the two signal beams from the OPAs. These excitation pulses are focused onto the sample at spot size of ~65 µm and overlapped with the 800-nm probe pulses (35 µm spot size). Their time delay dependent second harmonic intensity and polarization rotation are detected by a photo multiplier tube and a balanced detection scheme, respectively.

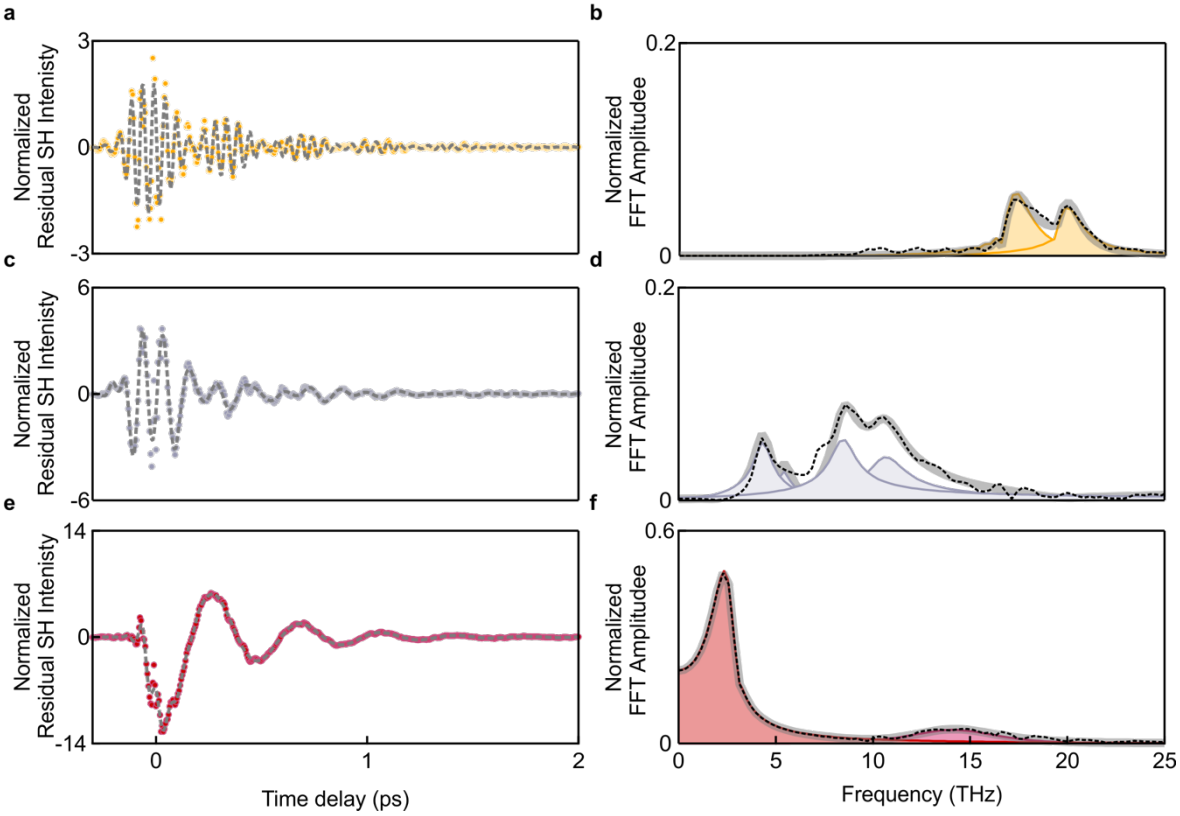

Fig. S2: Coherent oscillations in the time delay dependent second harmonic intensity from $YBa_2Cu_3O_{6.48}$, as shown in Fig. 4c of the manuscript for 7MV/cm excitation at 5 K, divided into three contributions and shown together with their Fourier amplitude spectra. Panels **a,b** show the apical oxygen phonons, panels **c**,**d** show the nonlinearly coupled infrared active phonons, and panels **e**,**f** show the Josephson Plasma modes. Experimental phonon oscillations (yellow and grey dots in a and c, respectively) are fitted by oscillators with frequencies constrained by infrared spectroscopy data (dashed lines).[3] Oscillations of the two Josephson plasma modes (experimental data as red dots in e) are best fitted by two oscillators at 2.3 and 14 THz (dashed line). In the Fourier amplitude spectra, the colored peaks highlight the respective contributions.

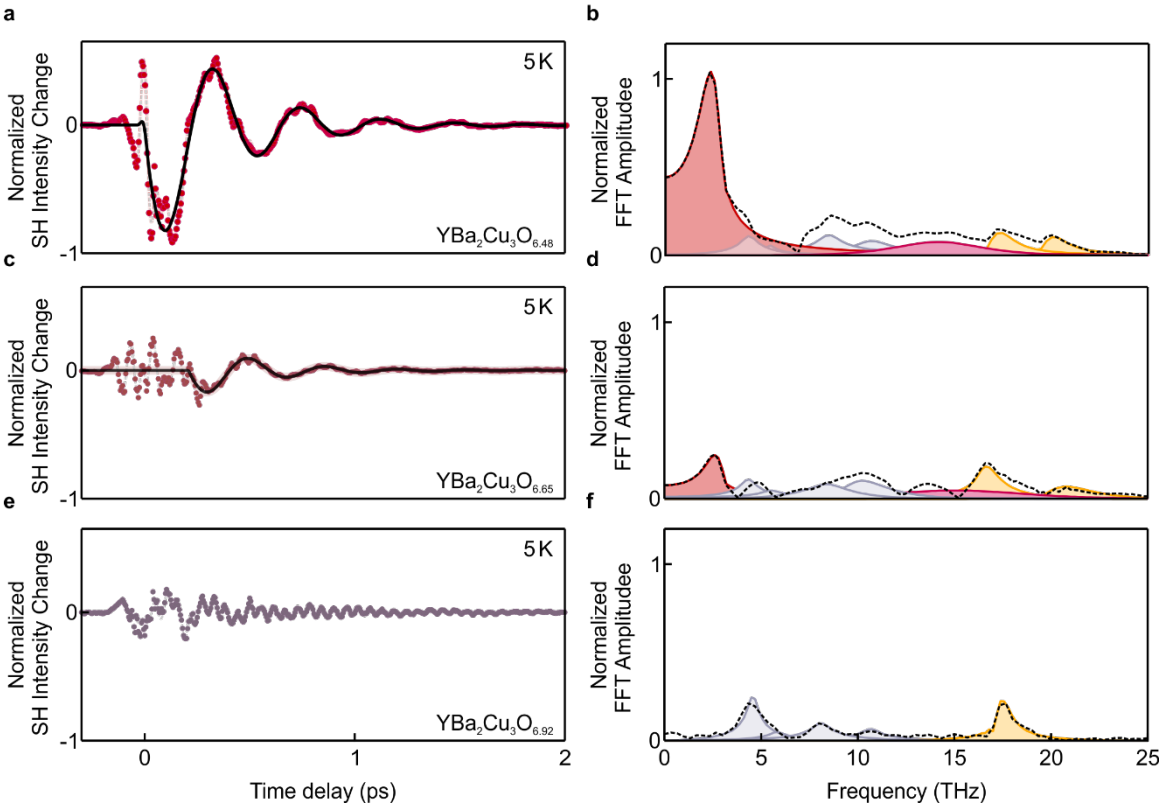

Fig. S3 Coherent oscillations in the time delay dependent second harmonic intensity of **a** $YBa_2Cu_3O_{6.48}$, **c** $YBa_2Cu_3O_{6.65}$ and **e** $YBa_2Cu_3O_{6.92}$, measured in the superconducting state at 5 K, together with corresponding Fourier amplitude spectra in **b, d, f**. Experimental data are plotted as red dots in panels a, c, e, together with the best fits to the data (light grey dashed lines) and the dominating low-frequency Josephson plasmon contribution (black solid line). The Fourier amplitude spectra include Josephson plasmons as red and magenta peaks, resonantly driven apical oxygen phonons as yellow peaks, and the nonlinear coupled infrared active phonons as grey peaks. Note the absence of the Josephson plasma oscillations in $YBa_2Cu_3O_{6.92}$. All experiments were performed with a peak electric field strength of 7 MV/cm.

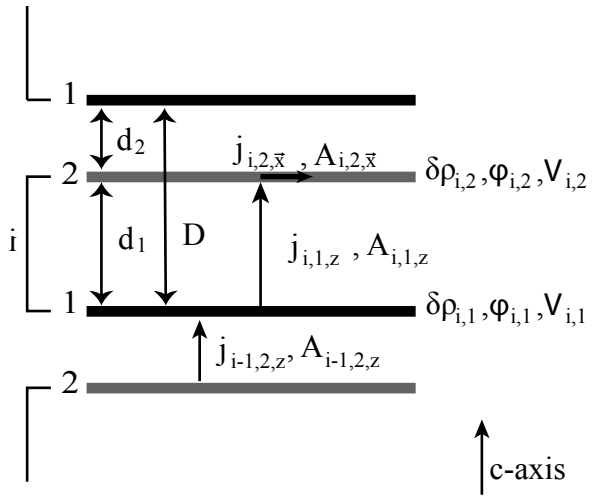

Fig. S4

Schematic drawing of a bilayer superconductor. Variables $\delta\rho_{i,\lambda}$, $\phi_{i,\lambda}$, $j_{i,\lambda,\vec{x}}$, and $A_{i,\lambda,\vec{x}}$ are defined within layer λ in unit cell i and describe condensate density fluctuations, phase of the order parameter, parallel component of the superfluid current, electrostatic potential, and in-plane vector potential respectively. Variables $j_{i,\lambda,z}$, and $A_{i,\lambda,z}$ are defined between the layers and correspond to interlayer Josephson current and out of plane component of the vector potential, respectively.

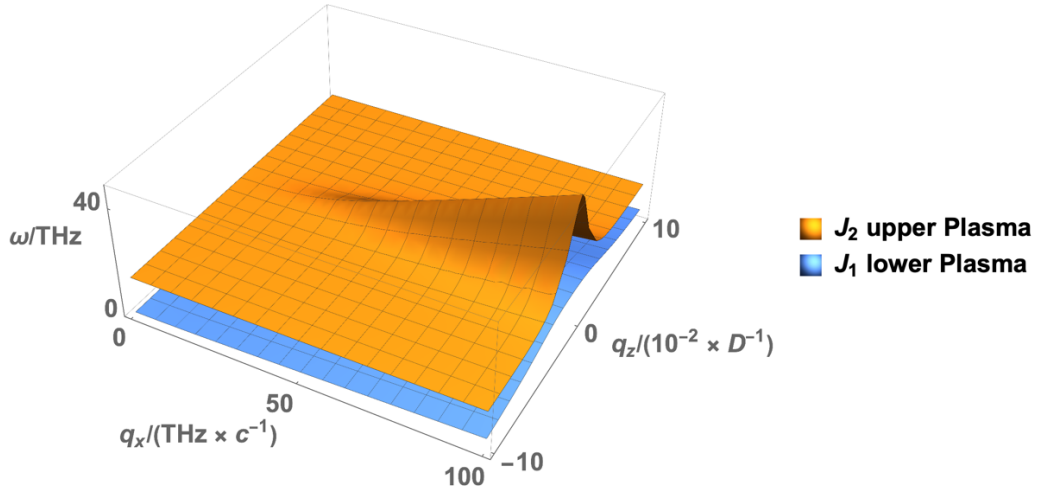

Fig. S5:

Dispersion relation of the two lowest energy modes of equations (10)-(12) in the $\{q_x, q_z\}$-plane. At $q_z = 0$, the upper plasmon is strongly hybridized with the original photon mode. This results in the energy of the mode increasing rapidly along the q_x axis with the slope approaching the speed of light. Away from $q_z = 0$ strong mixing with the photon is absent and the frequency of the mode decreases with increasing q_x.

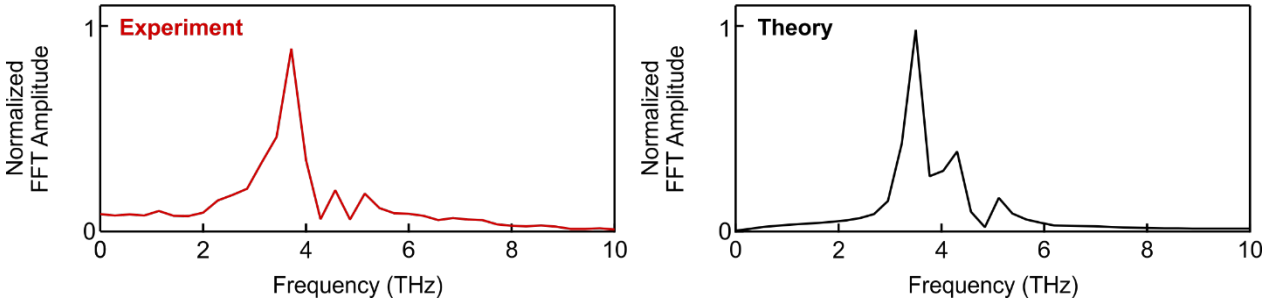

Fig. S6: Fourier amplitude spectrum of Raman active phonons in $YBa_2Cu_3O_{6.48}$, extracted from the time-resolved polarization rotation measurement of 800-nm probe pulses shown in Fig. 3b of the main text (left), and obtained from calculations of their third order nonlinear coupling to the resonantly driven apical oxygen phonons (right).

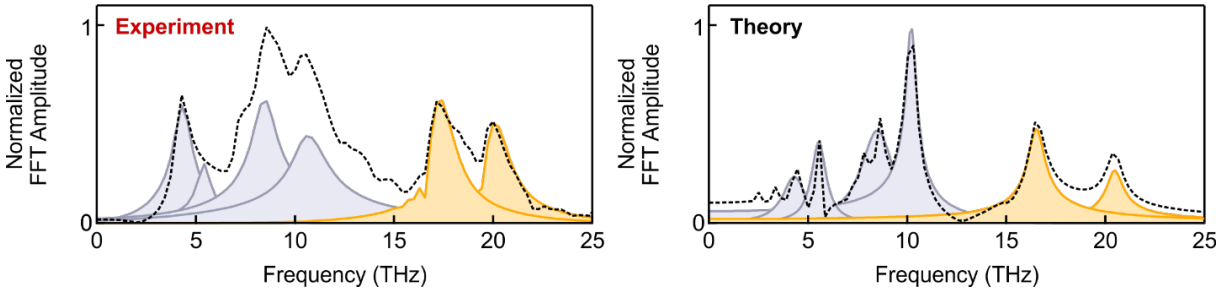

Fig. S7: Contributions of infrared active phonons to the Fourier amplitude spectrum of the time-resolved second harmonic intensity measurement, shown in Fig. 4d of the main text, are plotted on the left. The resonantly driven apical oxygen vibrations and nonlinear coupled lattice modes are shown as yellow and grey peaks, respectively. The Fourier spectrum obtained from calculations of the dynamics of the driven apical oxygen phonons and their fourth order coupling to the lower frequency phonons are shown in the right panel.

References (Supplementary Materials)

[44] S. I. Schlachter et al., Pressure effect and specific heat of $RBa_2Cu_3O_x$ at distinct charge carrier concentrations: Possible influence of stripes. *Int. J. Mod. Phys. B* 14, 3673 (2000).

[45] Y.X. Yan, E. B. Gamble Jr. & K. A. Nelson, Impulsive stimulated scattering: General importance in femtosecond laser pulse interactions with matter, and spectroscopic applications. *J. Chem. Phys.* 83, 5391-5399 (1985).

[46] R. Merlin, Generating coherent THz phonons with light pulses. *Solid State Commun.* 102, 207–220 (1997).

[47]M. Cardona, R. K. Chang, G. Güntherodt, M. B. Long and H. Vogt, Light Scattering in Solids II. Topics in Applied Physics (Springer, Berlin, Heidelberg, 1982).

[48] V. N. Denisov, B. N. Mavrin and V. B. Podobedov, Hyper-Raman scattering by vibrational excitations in crystals, glasses and liquids. *Physics Reports* 151, 1 (1987).

[49] Z. Cheng, Quantum field theory of hyper-Raman scattering in piezoelectric crystals. *Physical Review B* 66, 165101 (2002).

[50] D. Munzar, C. Bernhard, A. Golnik, J. Humlicek and M. Cardona, Anomalies of the infrared-active phonons in underdoped $YBa_2Cu_3O_y$ as evidence for the intra-bilayer Josephson effect. *Solid State Communications* 112, 365-369 (1999).

[51] L. N. Bulaevskii, M. Zamora, D. Baeriswyl, H. Beck, and John R. Clem. Time-dependent equations for phase differences and a collective mode in Josephson-coupled layered superconductors. *Phys. Rev. B* 50, 12831(1994).

[52] T. Koyama and M. Tachiki. I-v characteristics of Josephson-coupled layered superconductors with longitudinal plasma excitations. *Phys. Rev. B* 54, 16183 (1996).

[53] T. Koyama. Josephson plasma resonances and optical properties in high-tc superconductors with alternating junction parameters. *Journal of the Physical Society of Japan* 71, 2986 (2002)

[54] J. Okamoto, A. Cavalleri, and L. Mathey. Theory of enhanced interlayer tunneling in optically driven high-T_c superconductors. *Phys. Rev. Lett.* 117, 227001(2016).

[55] J. Okamoto, W. Hu, A. Cavalleri, and L. Mathey, Transiently enhanced interlayer tunneling in optically driven high-T_c superconductors. *Phys. Rev. B* 96, 144505 (2017).

[56] D. van der Marel and A. A. Tsvetkov, Transverse-optical Josephson plasmons: Equations of motion. *Phys. Rev. B* 64, 024530 (2001).

[57] M. Fechner and N. A. Spaldin, Effects of intense optical phonon pumping on the structure and electronic properties of yttrium barium copper oxide. Phys. Rev. B **94**, 134307 (2016).

[58] D. M. Juraschek, M. Fechner, and N. A. Spaldin, Ultrafast Structure Switching through Nonlinear Phononics. Phys. Rev. Lett. **118**, 054101 (2017).